
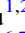













Long-term Monitoring of Didymos with the LCOGT Network and MRO after the DART Impact

Tim Lister¹ , Cora Constantinescu^{1,2,10} , William Ryan³ , Eileen Ryan³ , Edward Gomez⁴ , Liz Phillips^{1,2,10} ,
Agata Rożek⁵ , Helen Usher^{6,7} , Brian P. Murphy⁵ , Joseph Chatelain¹ , and Sarah Greenstreet^{8,9} 

¹Las Cumbres Observatory, 6740 Cortona Drive, Suite 102, Goleta, CA 93117, USA; tlister@lco.global

²Department of Physics, University of California, Santa Barbara, CA 93106-9530, USA

³New Mexico Institute of Mining and Technology/Magdalena Ridge Observatory, 801 Leroy Place, Socorro, NM 87801, USA

⁴Las Cumbres Observatory, School of Physics and Astronomy, Cardiff University, Queens Buildings, The Parade, Cardiff CF24 3AA, UK

⁵Institute for Astronomy, University of Edinburgh, Royal Observatory, Edinburgh, EH9 3HJ, UK

⁶The Open University, Walton Hall, Milton Keynes, MK7 6AA, UK

⁷The Faulkes Telescope Project, UK

⁸Rubin Observatory/NSF's NOIRLab, 950 N. Cherry Avenue, Tucson, AZ 85719, USA

⁹Department of Astronomy and the DIRAC Institute, University of Washington, 3910 15th Avenue NE, Seattle, WA 98195, USA

Received 2023 November 17; revised 2024 March 26; accepted 2024 April 11; published 2024 May 31

Abstract

The world's first planetary defense test mission was carried out in late 2022 by NASA's Double Asteroid Redirection Test (DART) mission. The main DART spacecraft, which was accompanied by the ASI-provided LICIACube cubesat, intentionally impacted Dimorphos, the smaller secondary of the near-Earth object binary system (65803) Didymos, on 2022 September 26. The impact released a large amount of ejecta, which, combined with the spacecraft's momentum, produced the observed 33 ± 1 minute period change that was subsequently observed from ground-based telescopes. The DART mission, in addition to having successfully changed the orbital period of Dimorphos, also activated the asteroid as a result of the impact but under known conditions, unlike other impacts on asteroids. We have conducted long-term monitoring over 5 months following the impact with the Las Cumbres Observatory Global Telescope (LCOGT) network and Magdalena Ridge Observatory (MRO). This was supplemented by almost 3 months of more sparsely sampled data, primarily from educational users of the LCOGT network during the period from 2022 July 5 to 2022 September 25, prior to the impact date of 2022 September 26. Here we report the observations of the Didymos system and DART impact ejecta with the telescopes of the LCOGT network from T+1.93 days to T+151.3 days after impact, and we study the evolving morphology of the ejecta cloud and evolving tail over the entire length of the data set. In addition, we combined these intensive data sets with the earlier sparse observations over the ~ 90 days prior to impact to derive a new disk-integrated phase function model using the H , G_1 , G_2 parameterization.

Unified Astronomy Thesaurus concepts: Asteroids (72); Near-Earth objects (1092); Optical astronomy (1776); Ejecta (453); Photometry (1234)

Supporting material: machine-readable tables

1. Introduction

The Double Asteroid Redirection Test (DART) mission was a technology demonstration mission that performed the world's first planetary defense test on an actual asteroid (Rivkin et al. 2021). The DART spacecraft, which had a mass of ~ 580 kg at the time of impact, crashed into asteroid Dimorphos, the smaller, ~ 150 m diameter secondary of the near-Earth object (NEO) Didymos, on 2022 September 26 at 23:14:24.183 UTC (Daly et al. 2023). Two of the principal aims of the DART mission were to change the orbital period of Dimorphos around Didymos in a measurable way and to measure the momentum enhancement factor β in order to quantify the amount of additional momentum imparted by the ejecta, over and above that which was provided by the DART spacecraft itself. These two aims were motivated by trying to understand and quantify the effect of

kinetic impacts on NEOs, with the long-term aim of gaining a deeper understanding about the feasibility and effectiveness of kinetic impactor deflection missions as possible tools for humanity to protect Earth against potential future asteroid impacts. The first goal of measuring the altered orbital period was shown to be successfully achieved by Thomas et al. (2023) from ground-based observations, including from the Las Cumbres Observatory Global Telescope (LCOGT) network. The second goal of measuring β was also achieved (Cheng et al. 2023), albeit with large errors bars that will be substantially improved when ESA's Hera mission (Michel et al. 2022) arrives at the Didymos system in 2026 to perform a full characterization of the system and assess the results of the DART impact.

In addition to the primary mission goals discussed above, the DART impact gave the opportunity to study collisional processes under controlled conditions that are well observed. There is ample evidence from craters, the dynamical structure of the asteroid belt and families, and the rubble pile nature of asteroids that collisions occur throughout the solar system and during its entire history, but the vast majority of evidence is indirect and from a long time in the past. There is a small but growing volume of evidence that some active asteroids are

¹⁰ Summer intern at LCO.

LAS CUMBRES OBSERVATORY GLOBAL TELESCOPE NETWORK

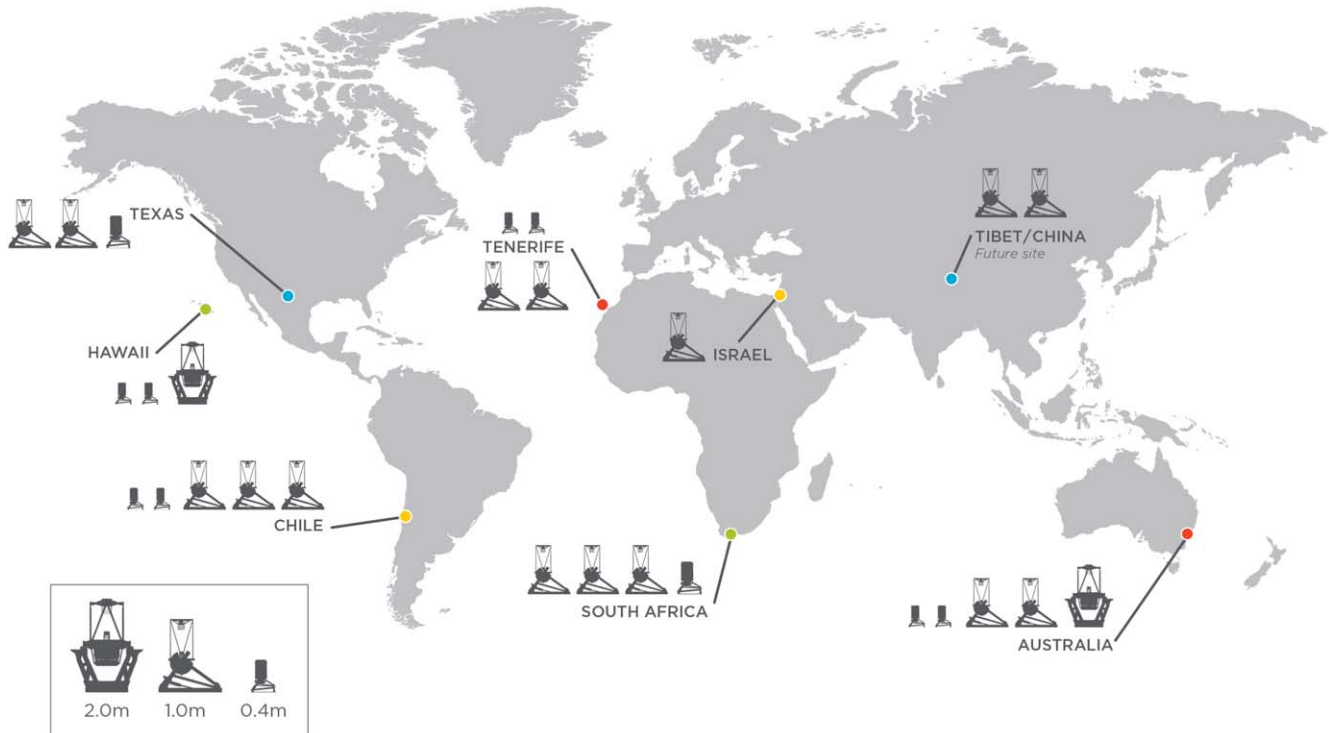


Figure 1. Network map of LCOGT facilities. The site in Israel does not have an imager and therefore did not participate in the DART observation campaign.

produced by collisions (e.g., Snodgrass et al. 2010; Hainaut et al. 2012). The impact of the DART spacecraft, with its known mass, velocity, and trajectory (Daly et al. 2023), provides a rare opportunity to study the activation of an asteroid from before the time of impact onward. As noted above, the DART impact occurred on 2022 September 26 23:14 UTC during the night for LCOGT’s South Africa site, allowing study with multiple telescopes of the LCOGT network. Initial results on the ejecta from Hubble Space Telescope (HST) imaging have been reported by Li et al. (2023) and over the first month by Kareta et al. (2023) and Rožek et al. (2023); in this paper we concentrate on the long-term monitoring observations of the Didymos system over 5 months that were obtained with the LCOGT network.

2. Observations with the LCOGT Network

The LCOGT network is a global network of 25 telescopes in three size classes at seven sites around the world (Brown et al. 2013) as shown in Figure 1. All of the telescopes are remote and robotic, and the network is scheduled as a whole in response to new observing requests submitted through the web-based Observing Portal or through an API interface. The global coverage of this network and the apertures of telescopes available make LCOGT ideal for both rapid response and long-term monitoring for follow-up and characterization of solar system objects in general and for NEOs in particular, including those of special interest such as Didymos.

The data analyzed in this paper come from several observing programs that were running on the 1.0 and 2.0 m telescope networks:

1. Time-of-impact observations from the night of 2022-09-26/27 using the LCOGT 1m+FLI instruments.
2. DART-contracted light-curve observations using the LCOGT 1m+Sinistro instruments.
3. Tail and ejecta monitoring observations using the LCOGT 1m+Sinistro instruments.
4. Additional Didymos observations taken by education users using the LCOGT 1m+Sinistro instruments and 2m+MuSCAT3 and Spectral instruments.

These will be described in more detail in the following sections, but the following general details are applicable to all the data sets. Didymos data were obtained from the LCOGT nodes located at the following sites:

1. Cerro Tololo Inter-American Observatory, District IV, Chile (three 1.0 m telescopes, LCOGT site code lsc, MPC site codes W85, W86, W87).
2. South African Astronomical Observatory, Sutherland, South Africa (three 1.0 m telescopes, LCOGT site code cpt, MPC site codes K91, K92, K93).
3. Siding Spring Observatory, NSW, Australia (two 1.0 m telescopes, MPC site codes Q63, Q64; 2.0 m telescope, LCOGT site code coj, MPC site code E10).
4. Haleakala Observatory, Maui, Hawaii (2.0 m telescope, LCOGT site code ogg, MPC site code F65).
5. McDonald Observatory, Fort Davis, Texas (two 1.0 m telescopes, LCOGT site code elp, MPC site codes V37, V39).
6. Teide Observatory, Canary Islands, Spain (two 1.0 m telescopes, LCOGT site code tfn, MPC site codes Z31, Z24).

A log of observations obtained with LCOGT is given in Table 2 in the Appendix. All the LCOGT 1.0 m telescopes are equipped with the Sinistro CCD optical imaging instruments, each containing a $4\text{ k} \times 4\text{ k}$ Fairchild CCD with $15\ \mu\text{m}$ pixels. The Sinistro imagers provide a $26'5 \times 26'5$ field of view with an unbinned pixel scale of $0''.389\ \text{pixel}^{-1}$. The Sinistro imagers are equipped with three filter wheels containing 21 filters in total (complete Bessell & Sloan/PanSTARRS sets, plus the PanSTARRS-w filter, equivalent to Sloan Digital Sky Survey (SDSS) $g' + r' + i'$, providing high throughput between 400 and 850 nm, and used for light curves). In addition to the main Sinistro imaging cameras, each 1 m telescope has an FLI CCD guider camera containing a 1024×1024 CCD with $13.5\ \mu\text{m}$ pixels. This gave a field of view of $5'8 \times 5'8$ with an unbinned pixel scale of $0''.34\ \text{pixel}^{-1}$ capable of imaging at up to a rate of 0.5 Hz.

2.1. Time-of-impact Observations

Although not part of the mission goals for the DART mission, and despite considerable uncertainty pre-impact (Fahnestock et al. 2022; Moreno et al. 2022) on what would be visible from ground-based observatories, we decided to take advantage of the multiple 1 m telescopes and fast frame rate cameras at LCOGT's South African node. We attempted multitelescope imaging of the evolution of the impact plume and ejecta after the DART spacecraft's impact into Dimorphos. We configured quasi-simultaneous observations using the FLI cameras, with each camera observing in a different filter (SDSS g' and i' , along with a broad bandpass clear filter) with a repeating pattern of $2 \times 2\text{ s}$, $2 \times 10\text{ s}$, and $2 \times 30\text{ s}$ exposures. (We describe the observations as "quasi-simultaneous" since each telescope and instrument were commanded to observe the same sequence of observations starting at the same time, but due to the differences in setup and processing times and lack of synchronization between the instruments, the start times of the similar exposures on the different instruments in the different filters differ by $\sim 1\text{ s}$.) The shortest (2 s) exposures were chosen as a balance and compromise based on the signal-to-noise ratio achievable in the limited amount of pre-impact test data available, the highly uncertain predictions of the post-impact magnitude increase, and the need to maintain reasonable open-shutter efficiency, given the FLI camera dead time of $\sim 2\text{ s}$. Observations coming back in near real time showed that a large cloud of expanding fast-moving ejecta had been produced as a result of the impact of the DART spacecraft into Dimorphos, contrary to and exceeding the predictions. This observation sequence was continued until 2022-09-27 01:20 UTC ($\sim 2\text{ hr}$ after impact), when the magnitude of the Didymos system had visibly declined from the peak and the $2 \times 2\text{ s}$ exposures were dropped.

This data set has been combined with others taken from the African continent (Fitzsimmons et al. 2023) and will be analyzed in greater detail by A. Fitzsimmons et al. (2024, in preparation), and we only focus on the broad bandpass clear filter in the remainder of this paper.

2.2. Light-curve, Tail, and Ejecta Monitoring Observations

All of the light-curve and tail monitoring images were obtained in 1×1 binning mode with a PanSTARRS-w filter (equivalent to SDSS $g' + r' + i'$), which provided high throughput without including the highly variable water bands

in the red/near-IR. For all LCOGT DART data presented here, the telescopes were tracking at half Didymos's on-sky ephemeris rate throughout the observations. Individual exposure times ranged from 27.5 to 150 s during the DART light-curve observations.

We also used the global LCOGT network of telescopes for nightly cadence observations to monitor the evolving ejecta brightness and tail development every $\sim 8\text{ hr}$ over a period of 5 months from 2022 October to 2023 February. Both the light-curve and tail monitoring observations obtained by us were scheduled using the NEOexchange Target and Observation Manager (TOM; Lister et al. 2021) system to submit several weeks of cadence monitoring observations for each site in the network.

2.3. Education User Data

The regular cadence was supplemented by additional data obtained through the Comet Chasers school outreach program and also additional educational data that were obtained in either w or r' filters and with a sufficient number of exposures and with long enough exposure times that the tail was likely to be detectable. Some of these data came from the 2.0 m Faulkes Telescope North (FTN; MPC site code F65) using the MuSCAT3 four-channel imager (Narita et al. 2020). The MuSCAT3 instrument at FTN makes use of dichroics to provide simultaneous four-color imaging in the $g'r'i'z_s$ filters. Three different (but very similar) Princeton Instrument CCD cameras are used in MuSCAT3: Pixis 2048_eX cameras in the g' and i' channels, a Pixis 2048B camera in the r' channel, and a Sophia 2048BR deep depletion camera in the z_s channel. All the Pixis 2048 and Sophia 2048 cameras have 2048×2048 pixel CCD cameras with $13.5\ \mu\text{m}$ pixels giving $0''.27\ \text{pixel}^{-1}$ after the focal reducer; the cameras' main differences are in the quantum efficiency, which is optimized for each channel, the readout noise, and full well capacity.

In addition to the FTN MuSCAT3 data, a small amount of the educational user data used the Spectral camera on the 2.0 m Faulkes Telescope South (FTS; MPC site code E10). The camera uses a Spectral Instruments CCD camera with a $4\text{ k} \times 4\text{ k}$ Fairchild CCD with $15\ \mu\text{m}$ pixels. This gives a pixel scale of $0''.304\ \text{pixel}^{-1}$ in the 2×2 binning mode in which it is operated.

3. Observations with Magdalena Ridge Observatory

The Magdalena Ridge Observatory (MRO) fast-tracking 2.4 m telescope (MPC site code H01) is located at an elevation of 3250 m in the Magdalena Mountains near Socorro, New Mexico. All of the MRO images were acquired with the MRO2K CCD optical imager, which consists of an Andor iKon-L 936 camera operating at 188K and utilizes a 2048×2048 back-illuminated e2V CCD with $13.5\ \mu\text{m}$ pixels. The unbinned pixel scale is $0''.13\ \text{pixel}^{-1}$, yielding a $4'5$ field of view. Images were acquired in 4×4 binning mode while tracking on Didymos to maximize its signal. Observations early in the apparition were made using either the Bessell R or V filter and changed to a broadband VR filter later as it faded. Exposure times ranged from 15 to 150 s throughout the apparition. A table of observation details for the MRO data is given in Table 3 in the Appendix.

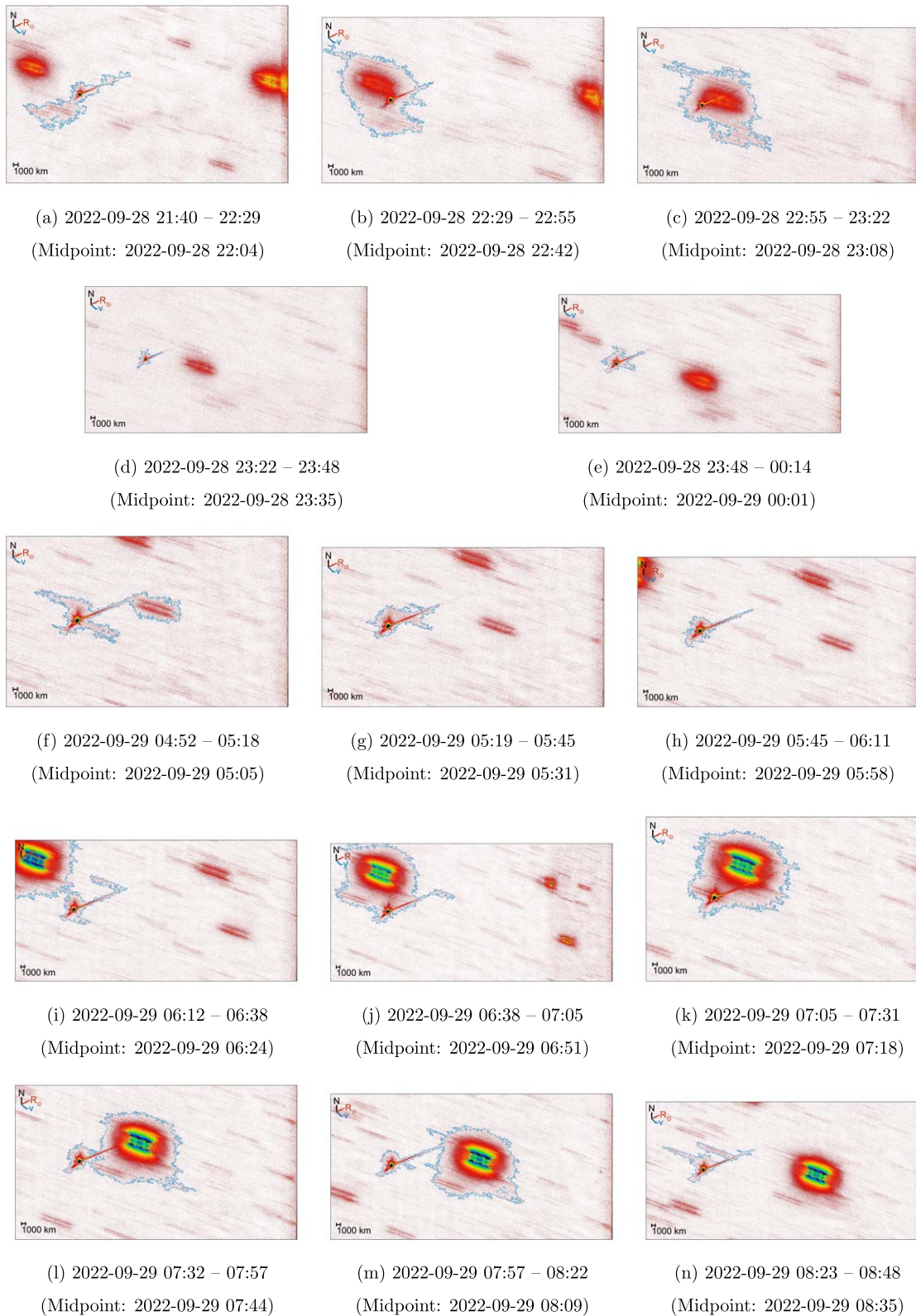


Figure 2. (a) Median-combined images stacked on Didymos's motion from 2022-09-28–29 (first “night” of LCOGT observations post-impact), along with the outline of the NoiseChisel detection for Didymos's tail and ejecta (blue outline). The arrows show the direction of the celestial north pole (black), the position angles of the Sun-to-target radius vector (orange), and the negative of the targets' heliocentric velocity vector (blue). The first five images are from the LCOGT CPT site (South Africa) and were taken in deteriorating sky conditions; the remainder are from the LCOGT LSC site (Chile). The time range under each figure is from the start of the first exposure to the end of the last exposure in the stack, given in UTC.

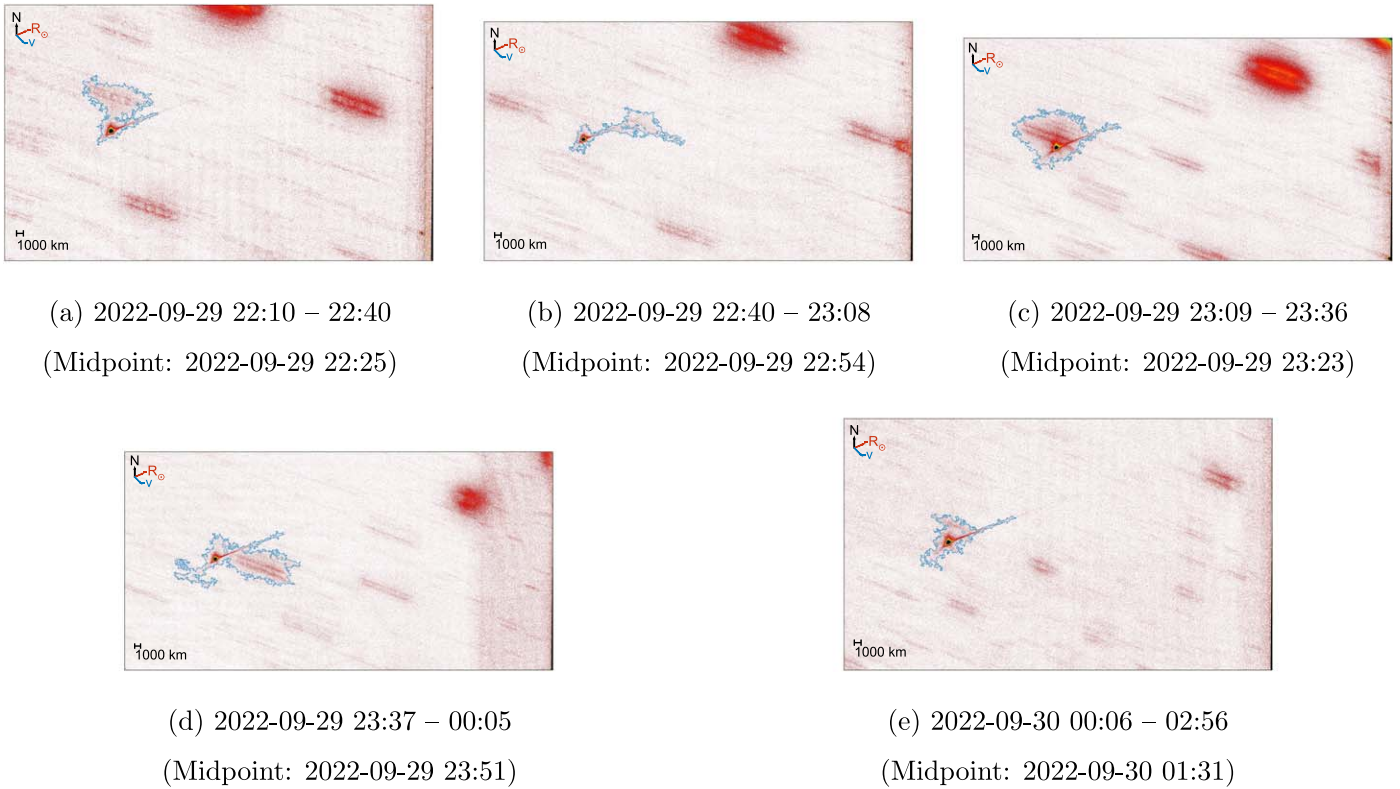


Figure 3. Median-combined substack images of Didymos from 2022-09-30 (second “night” of LCOGT observations post-impact) from the LCOGT CPT (South Africa) site. Labeling and other details are as in Figure 2.

4. Data Reduction

4.1. LCOGT Data Processing

The reduction of the Sinistro images followed a two-step process. Initial reduction to basic calibrated data (BCD) products involving bias and dark subtraction, flat-fielding, and astrometric fitting was performed automatically within minutes of readout of the frame by the LCOGT BANZAI pipeline (McCully et al. 2018). The BCD were then automatically retrieved from the LCOGT Science Archive in AWS and pipeline processed through the Photometry Pipeline (PP; Mommert 2017) and NEOexchange (NEOx; Lister et al. 2021) pipelines.

Both pipelines use Source-Extractor (Bertin & Arnouts 1996) to extract sources from the image and SCAMP (Bertin 2006) to perform the astrometric registration to the Gaia DR2 catalog (Gaia Collaboration et al. 2018) and then calibrated against the PanSTARRS DR1 catalog (Flewelling et al. 2020) or the Gaia DR2 catalog, depending on the decl. of Didymos at the time of the observations. This zero-point calibration within the NEOx pipeline was performed using the *calviacat* (Kelley & Lister 2022) package. For the light-curve data, a preliminary reduction was generally done with the PP, which automatically performs measurements using Source-Extractor through 20 different apertures in order to perform a curve-of-growth analysis. This was done in order to derive an optimal aperture radius for the main NEOx reductions and to act as a cross-check on the reductions. For the purposes of the tail monitoring, all the data from the light curve, tail ejecta

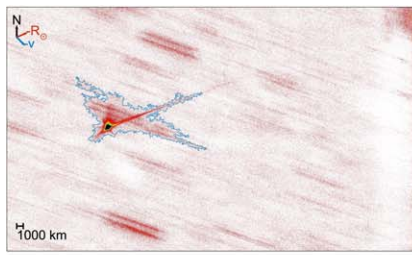
monitoring, and educational users (data sets 2–4 in Section 2) were systematically re-reduced using the NEOx pipeline to produce photometry in 11 equally spaced apertures of radius $1''$ – $10''$. These were then converted to the aperture diameters in pixels needed by Source-Extractor by the use of a mean Sinistro pixel scale of $0''.389635 \text{ pixel}^{-1}$.

Due to the low galactic latitude of Didymos in the early 2022 October–November data and the variable and differential reddening of the field stars, we did not use the features of either PP or *calviacat* to restrict the field stars to having solar-like colors. Similarly, to maintain consistency across the entire 5-month data set over the wide decl. range (decl. $\sim -36^\circ \dots +31^\circ$) covered by Didymos, we used the Gaia DR2 catalog for photometric calibration since parts of the data set were below the decl. range covered by the more accurate PanSTARRS DR1 catalog.

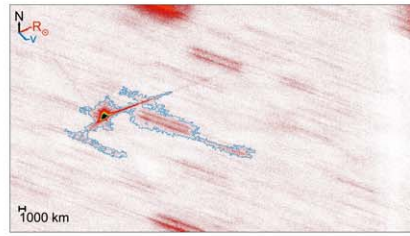
4.2. MRO Processing

The initial reduction of the MRO images to BCD products consisted of employing standard dark, bias, and flat-field correction techniques. This was carried out by WR and ER using custom scripts employing the IRAF (Tody 1986) *imcombine* and *imarith* tasks. These calibrated data products were then archived at the DART SOC.

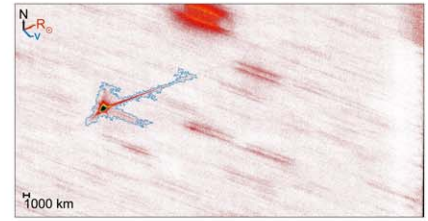
These BCD products were retrieved from the DART SOC, and then the metadata details for the nights and frames of data were ingested into the NEOx database. With the addition of a new routine to describe the mapping of fixed values and MRO-specific FITS header keywords to NEOx’s generalized header



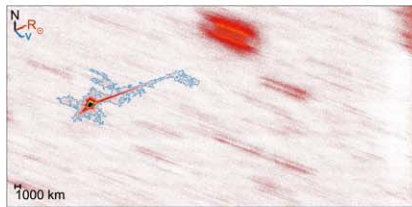
(a) 2022-09-30 03:52 – 04:19
(Midpoint: 2022-09-30 04:06)



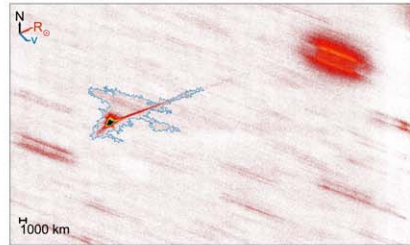
(b) 2022-09-30 04:20 – 04:46
(Midpoint: 2022-09-30 04:33)



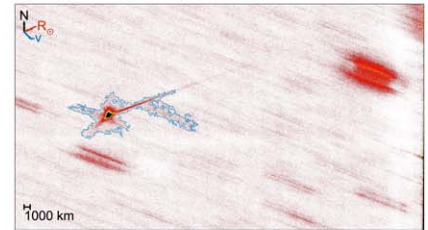
(c) 2022-09-30 04:47 – 05:13
(Midpoint: 2022-09-30 05:00)



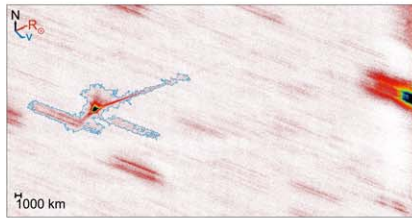
(d) 2022-09-30 05:14 – 05:41
(Midpoint: 2022-09-30 05:27)



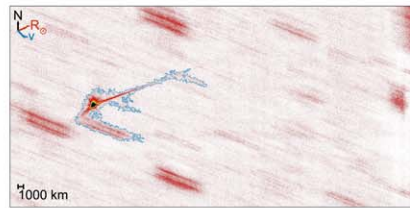
(e) 2022-09-30 05:41 – 06:08
(Midpoint: 2022-09-30 05:55)



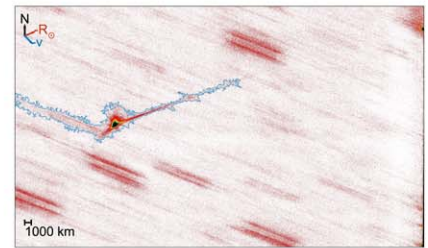
(f) 2022-09-30 06:09 – 06:36
(Midpoint: 2022-09-30 06:22)



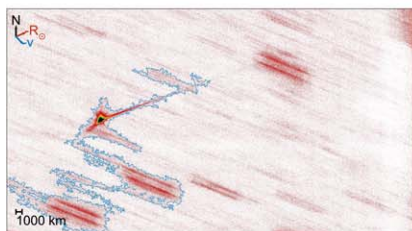
(g) 2022-09-30 06:36 – 07:03
(Midpoint: 2022-09-30 06:49)



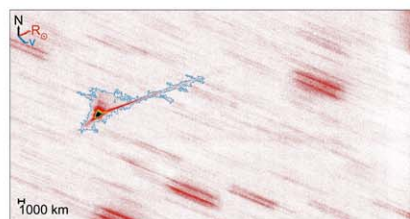
(h) 2022-09-30 07:03 – 07:30
(Midpoint: 2022-09-30 07:17)



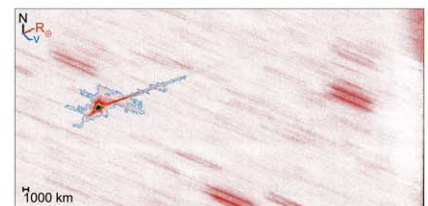
(i) 2022-09-30 07:31 – 07:58
(Midpoint: 2022-09-30 07:44)



(j) 2022-09-30 07:58 – 08:24
(Midpoint: 2022-09-30 08:11)



(k) 2022-09-30 08:24 – 08:50
(Midpoint: 2022-09-30 08:37)



(l) 2022-09-30 08:51 – 09:17
(Midpoint: 2022-09-30 09:04)

Figure 4. Median-combined substack images of Didymos from 2022-09-30 (second “night” of LCOGT observations post-impact) at the LCOGT LSC (Chile) site. Labeling and other details are as in Figure 2.

concepts and a new initial pipeline stage to create an initial WCS, it was possible to reduce all the data through the same NEOx pipeline described in Section 4.1 to perform the astrometric fitting. This enabled the use of the same motion stacking and morphology analysis procedures (see Section 4.3) for the deeper (but smaller-field-of-view) MRO data as for the LCOGT data.

4.3. Stacking and Tail Morphology Processing

In order to investigate the evolving tail morphology and ejected material around the Didymos–Dimorphos system, we constructed deeper stacks using the `Gnuastro` software suite (Akhlaghi & Ichikawa 2015; Akhlaghi 2018). These stacks were created using both light-curve data and tail and ejecta

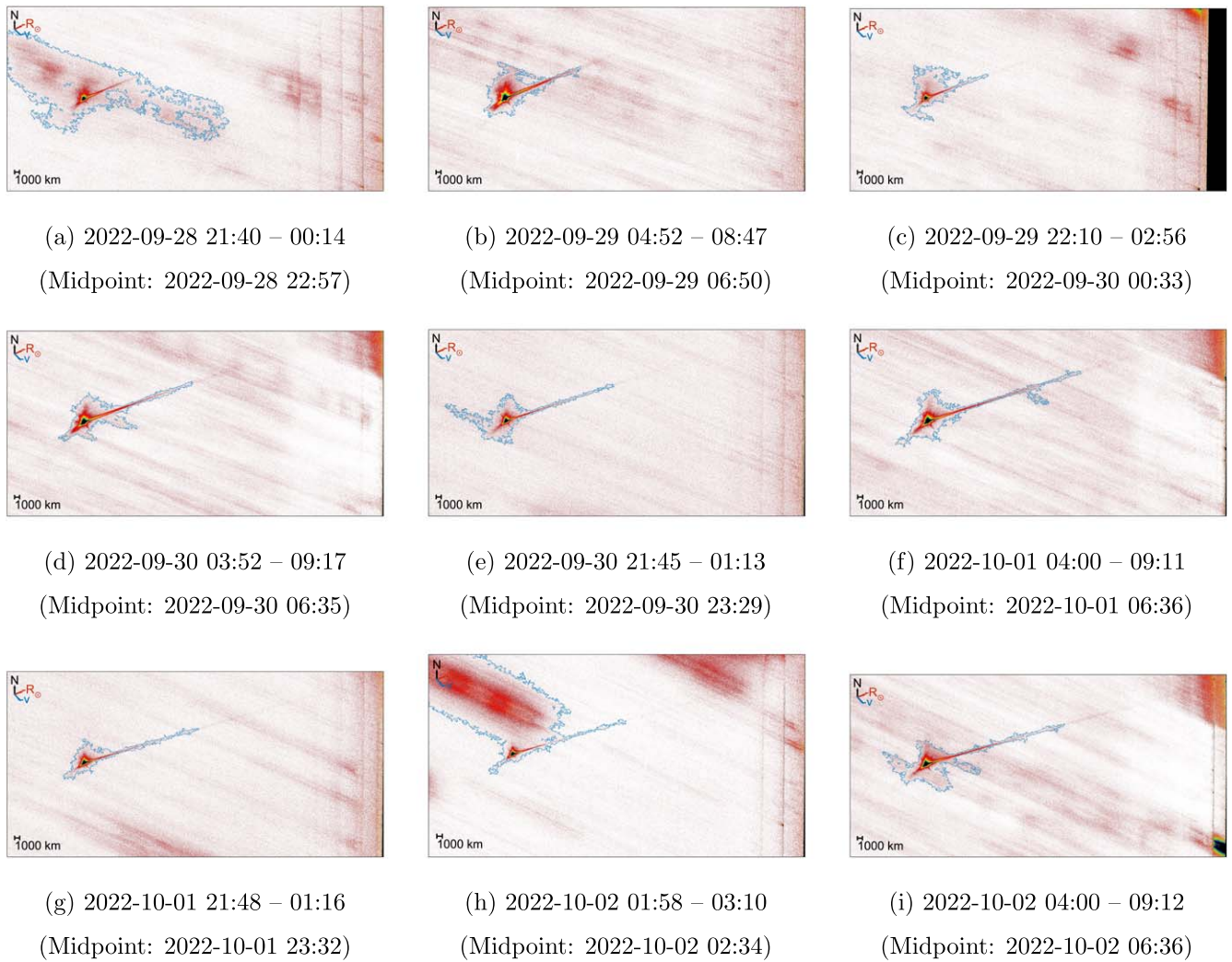


Figure 5. Median-combined stacked images of Didymos from 2022-09-28 to 2022-10-02 at the LCOGT CPT (South Africa) and LSC (Chile) sites.

Table 1
Table of Observations of Tail Length for (65803) Didymos with LCOGT and MRO

Stack Midpoint (UTC)	R_{\odot} (au)	Δ (au)	α (deg)	Tail Length (NC)		Tail Length (Man.)		Ratio
				(arcsec)	(km)	(arcsec)	(km)	
2022-09-28 22:57	1.04	0.07	56.2	237.3	12,665	272.4	14,538	0.87
2022-09-29 06:50	1.04	0.07	56.6	328.5	17,466	503.9	26,792	0.65
2022-09-30 00:33	1.04	0.07	57.7	273.6	14,440	611.1	32,253	0.45
				⋮				
2023-02-17 08:47 (MRO)	1.50	0.61	26.3	109.5 ^a	48,709 ^a	124.8 ^{+c}	55,543 ^{++c}	0.88
2023-02-25 05:32 (MRO)	1.54	0.70	28.8	121.7 ^a	61,657 ^a	110.7 ^a	56,086 ^a	1.10
				Tail Monitoring Blocks				
2023-01-25 23:02 (T)	1.38	0.41	15.0	⋮	⋮	101.6-	30,260-	⋮
				⋮				
2023-02-16 02:36 (T)	1.49	0.60	25.8	⋮	⋮	⋮	⋮	⋮
2023-02-20 06:48 (T)	1.52	0.64	27.3	⋮	⋮	⋮	⋮	⋮
2023-02-23 02:17 (T)	1.53	0.67	28.2	⋮	⋮	⋮	⋮	⋮

Notes. Each row represents a single-night, single-site, single-telescope light curve. The columns list the observing circumstances on a given night, the midpoint of the stack, the heliocentric (“ R_{\odot} ”) and geocentric (“ Δ ”) distances measured in AU, the solar phase angle (“ α ”), and the tail lengths measured by NoiseChisel (denoted by ‘NC’) and manually (denoted by ‘Man.’) in units of both arcsec and projected distance on the image, along with the ratio between the two methods (Length(NC)/Length(Man.).

^a Poor conditions.

⁻ Length measurement uncertain/lower limit due to obstruction.

⁺ Length measurement is a lower limit.

(This table is available in its entirety in machine-readable form.)

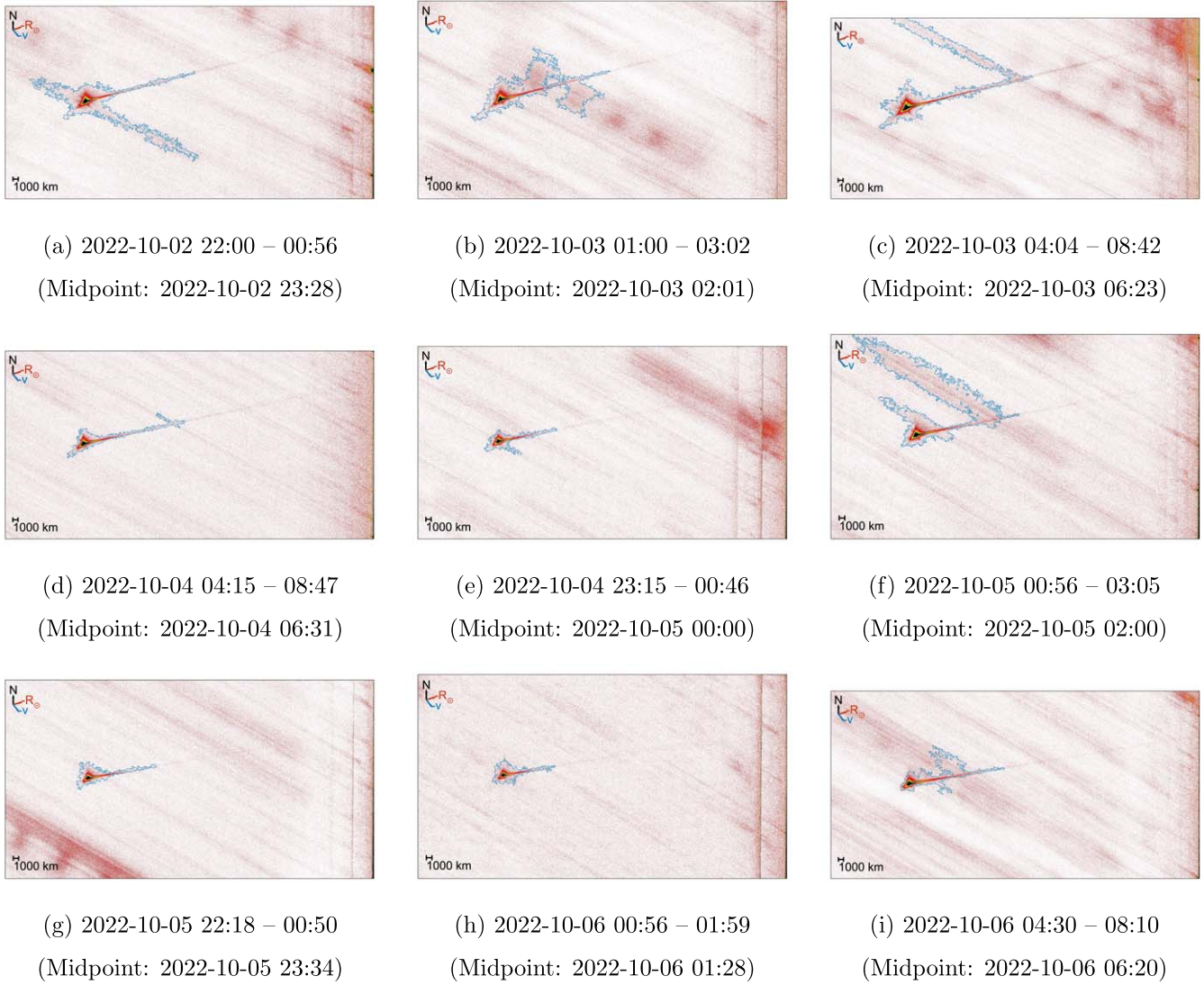


Figure 6. Median-combined stacked images of Didymos from 2022-10-02 to 2022-10-06 from the LCOGT network.

monitoring data. In order to produce stacks that have similar total exposure times, the light-curve observations were split into groups that were able to be stacked independently of each other.

Before stacking, we used `NoiseChisel` (Akhlaghi 2019; also from the `Gnuastro` suite) to create sky-subtracted versions of our images, and then each image was cropped to a size of 3769×1821 pixels. (The exceptions to this size were the MRO data, where 511×511 pixels was used owing to the smaller image sizes, and one educational user data set that came from the Spectral camera on FTS, which also had a smaller imager size and where 2045×1821 pixels was used).

The R.A., decl. position of Didymos was calculated at the time of each frame, transformed to a CCD x, y position using the WCS and then offset by $\pm 30\%$ of the image width (with the sign of the shift depending on whether the data came from a Northern or Southern Hemisphere LCO telescope with north either up or down in the images) in pixels, and retransformed to a new R.A., decl. position for the center of the crop. This was done in order to crop the images such that Didymos was off to the side to maximize the measurable tail extent, while not losing any potential extended structure around

Didymos off the edge of the resultant stack. Following cropping, the images were then stacked in such a way to try to blur the background stars: For each group of images to be stacked, N substacks were produced by combining every N th image in the group (in this step, the number N was decided based on the speed of Didymos and the exposure time of the frames). Then, all the substacks were recombined into one final stack. Following the stacking process, we used `NoiseChisel` once again on each stack to extract the signal from extended sources such as Didymos and the tail from out of the noise. The resulting stacked images are shown in Figures 2–10 for the LCOGT data and Figures 11 and 12 for the MRO data.

5. Analysis

5.1. Ejecta Production Analysis

We estimated the acceleration of fine dust grains from solar radiation pressure using the following equation:

$$a_{\text{srp}} = \frac{3L_{\odot}}{16\pi c R_{\odot}^2 \rho r} Q_{\text{srp}},$$

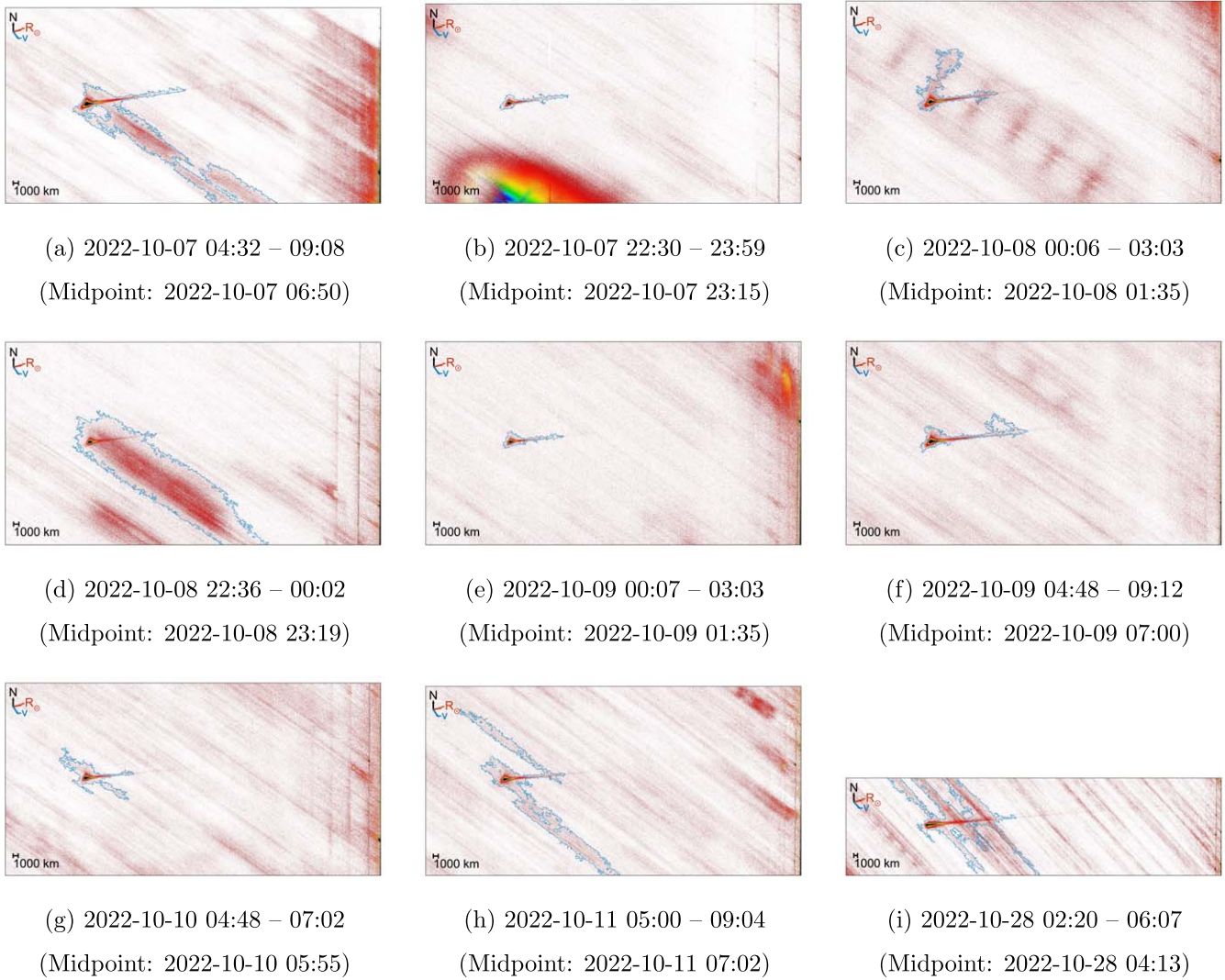


Figure 7. Median-combined stacked images of Didymos from 2022-10-07 to 2022-10-28 from the LCOGT network.

where the density ρ is taken as 2750 kg m^{-3} from the latest version of the DART Design Reference Asteroid (Chabot et al. 2024), the coefficient Q_{srp} is ≈ 1 , and the solar distance R_{\odot} is taken as a constant of value 1.04 au for the time of our first substack from the LCOGT CPT site.

Taking r as an independent variable, we used this acceleration to calculate the projected distance that a dust grain had been displaced between the time of DART’s impact and the time of our first stack (assuming zero initial velocity with respect to Didymos). We find that grains of radius $r = 1 \mu\text{m}$, typical of cometary coma, would have been accelerated to a projected distance of $\sim 304''$ in the ~ 1.95 days between the time of impact and our first stack, which is clearly well outside any of our photometric apertures. Since the acceleration due to the solar radiation pressure scales linearly with the dust radius, smaller dust grains would have been accelerated to even greater distance in the same time, whereas larger dust grains will not have traveled as far. For example, $10 \mu\text{m}$ grains will have traveled a projected distance of $\sim 30''$, and much smaller, very fine $0.1 \mu\text{m}$ grains would have very rapidly traveled $\sim 3040''$ ($\sim 50''$), which is almost twice the LCOGT Sinistro field of view. This is consistent with the very rapid evolution and material leaving the field of view seen in the higher-resolution

but much smaller field of view HST (Li et al. 2023) and VLT +MUSE (Opatom et al. 2023) observations.

Using the alternative density of 2400 kg m^{-3} assumed by Cheng et al. (2023), we found that grains of radius $r = 1 \mu\text{m}$ produced a minimal difference of $348''$ at the time of the first stack of our data compared to the above value and also when compared to a value of $279''$ using the 3000 kg m^{-3} typical of S-type asteroids, assumed by Rožek et al. (2023), with additional confirmation of the S-type classification coming from photometric colors (Lin et al. 2023).

The length of Didymos’s tail in our first stack (Figure 2(a)) was measured manually as $165''$, which corresponds to a dust grain of radius $1.84 \mu\text{m}$ assuming a density of 2750 kg m^{-3} . This indicates that dust of the expected $\sim 1 \mu\text{m}$ size is compatible with producing tail lengths of the sizes seen by the start of our observations and as seen by other observers in the Southern Hemisphere (Rožek et al. 2023).

5.2. Tail Length Analysis

We performed measurements of the estimated tail length on the final stacks resulting from light-curve observation blocks until the end of these observations in 2023 January (LCOGT)

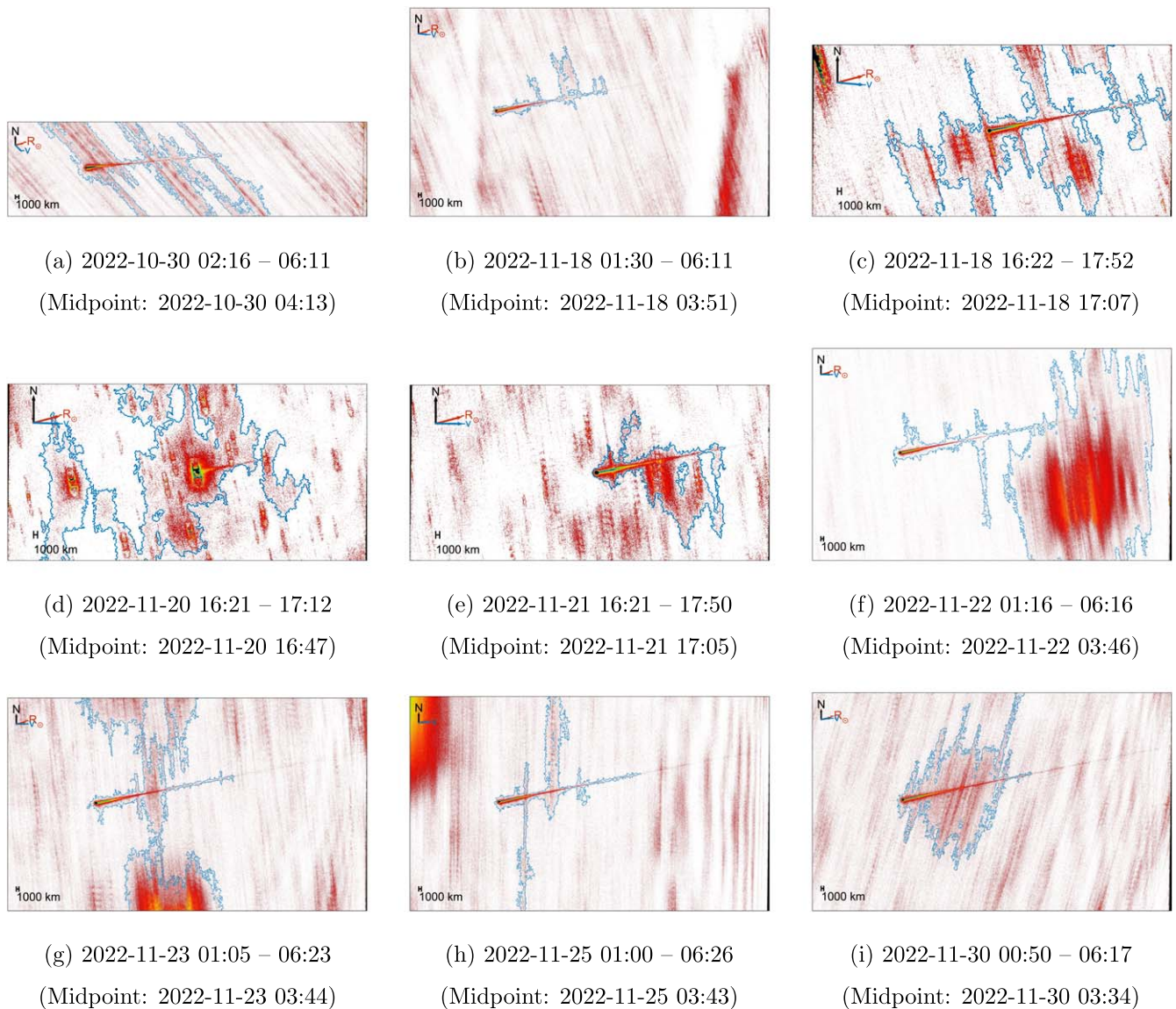


Figure 8. Median-combined stacked images of Didymos from 2022-10-30 to 2022-11-30 from the LCOGT network.

and 2023 February (MRO), and these 60 data sets are shown in the first part of Table 1. Following this time at the end of 2023 January when observations of the longer LCOGT light-curve blocks ceased, we made the same measurements on the shorter tail monitoring blocks for an additional 22 data sets. An additional 124 stacked tail monitoring data sets taken during the time of the light-curve observations (2022 September 28–2023 January 25) were not measured since they reached a shallower limiting magnitude than the concurrent light-curve blocks and therefore would not add additional information on the tail length. For each of the 82 tail stack data sets, the measurements were made in two ways: (1) by manual measurements of the extent of the NoiseChisel detection around Didymos in the direction of the Sun-to-target radius vector, which, as shown in Figure 5, aligns with the tail direction; and (2) by manual measurements on the stacked images through by-eye estimation of where the tail appeared to end. The results of these measurements are shown in Table 1, along with the ratio of the two measurements. In some cases, no measurement of the tail in the stacked image or detectable by NoiseChisel was possible, and these are indicated by

ellipses in the table. In other cases, the measurable tail length was curtailed by a bright star or extended off the stacked image, leading to uncertainty or a lower limit on the tail length; these are denoted by a minus or plus sign, respectively, after the measurements. Finally some observations were taken under poor conditions of thin cloud and/or moonlight, which also leads to an underestimate of the tail length; these are denoted by footnote a in the table.

We plot the measured manual (projected) lengths of the tail, along with the lower limits from those data sets where the tail extended off the length of the edge of the chip or the measurement was truncated by a star trail, in Figure 13. This shows that the tail length grew rapidly over the first ~ 10 days to $\sim 60,000$ km before observations and tail length measurements were hampered by the 2022 October 9 Full Moon, which will lead to a brighter background and shorter measured tail lengths during the period around the full moon. Following the 2022 October full moon, the projected tail length continued to increase over the following 2 months, albeit at a slower rate. The projected tail length reached a maximum extent of $\sim 160,000$ km in our data during 2022 December–2023

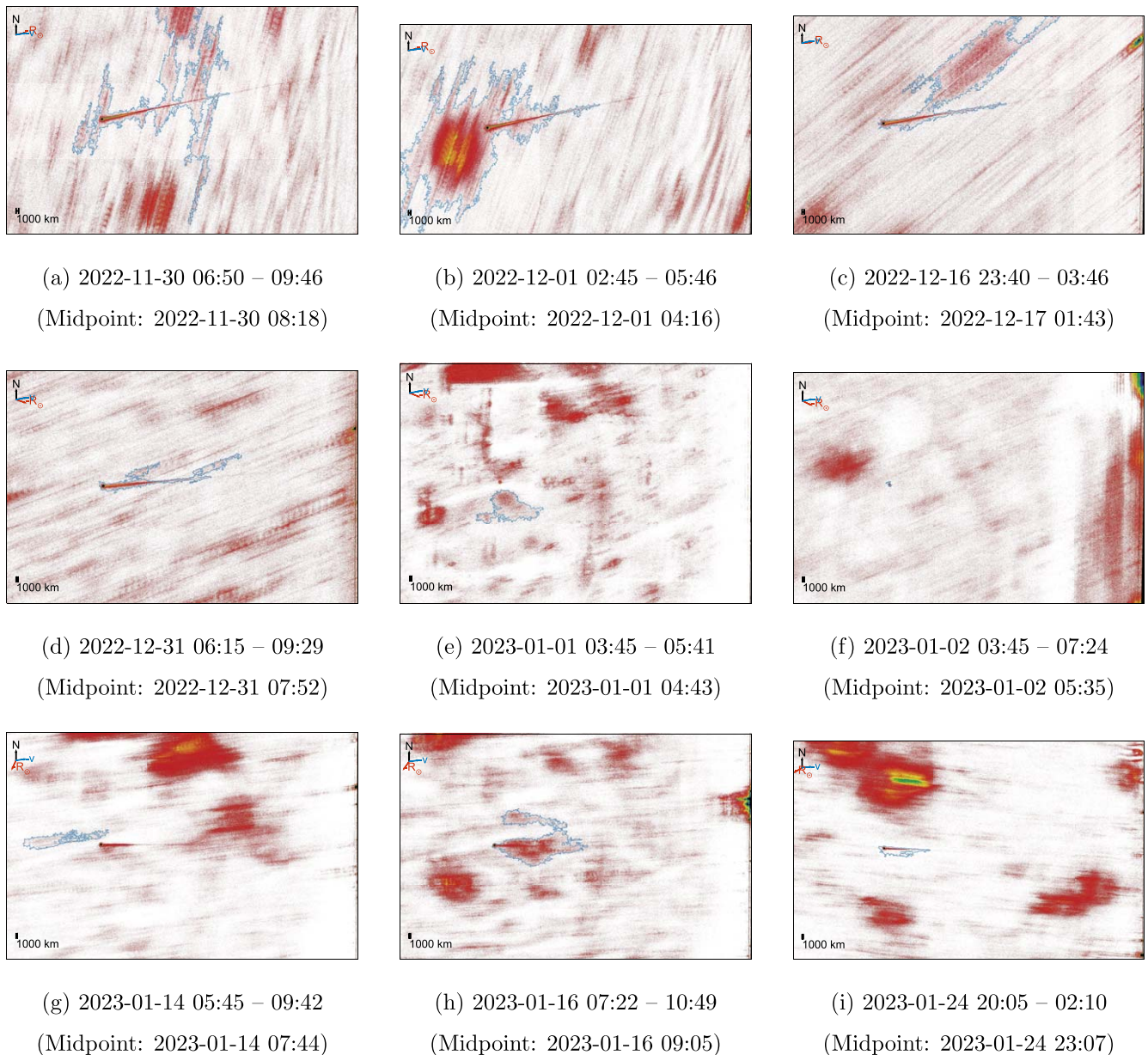


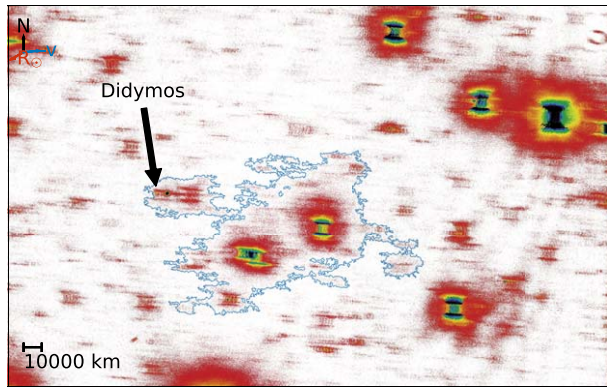
Figure 9. Median-combined stacked images of Didymos from 2022-11-30 to 2023-01-24 from the LCOGT network.

January before declining owing to a lower value and then slowly rising again. This is due to the effect of projection of the tail length as the viewing geometry, as indicated by the phase angle, undergoes a rapid decline to a minimum on 2023-01-10 ($T \sim +105$ days after impact) before rising again (see, e.g., Figure 14).

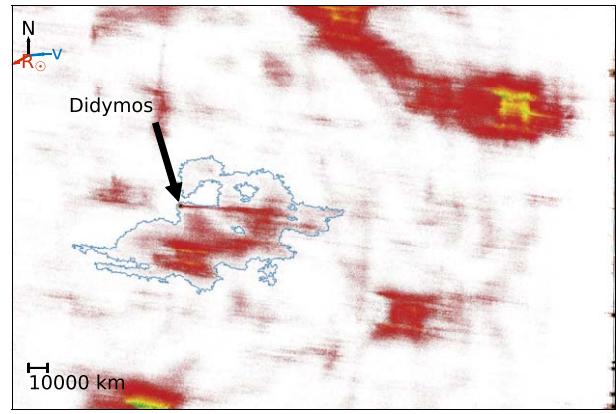
Comparing the tail lengths measured via the two methods of measuring the NoiseChisel detection around Didymos with the manually measured tail length and their ratio (final column of Table 1 and plotted in Figure 15) reveals no clear trend to over- or underprediction of manually measured tail length from the NoiseChisel software. Excluding the small spike of tail data sets with ratio ~ 1 produced by the MRO data sets that have a strong tail signal extending well off the edge of the CCD, which is much easier for NoiseChisel to detect, there is some preference for a ratio ~ 0.4 – 0.6 , but this is far from

being a “constant” correction factor that could be employed automatically in an automated pipeline.

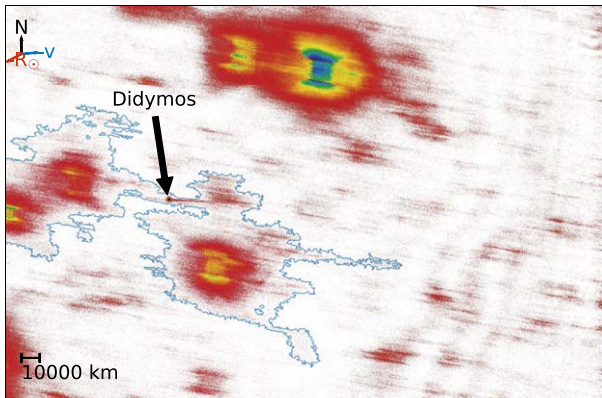
Examining the Didymos detection contours in the stacked images in Figures 5–12 reveals many instances where the NoiseChisel detection is contaminated through overlap with background (stellar) sources that have been trailed through the combination of the moving object tracking at the telescope and the shift and stack procedure to enhance the tail signal. There is some evidence, as would be expected, that this is worse during $\sim 2022-10-15$ – $2022-11-10$, when Didymos was at low galactic latitude and higher star density, but also when the rate of sky motion was low as in 2023 (see Figure 16). It is possible that this situation could be improved by additional optimization of the stacking process by making it adaptive to the rate of motion and exposure length and therefore the length of the stellar trails; this is beyond the scope of the current work, however.



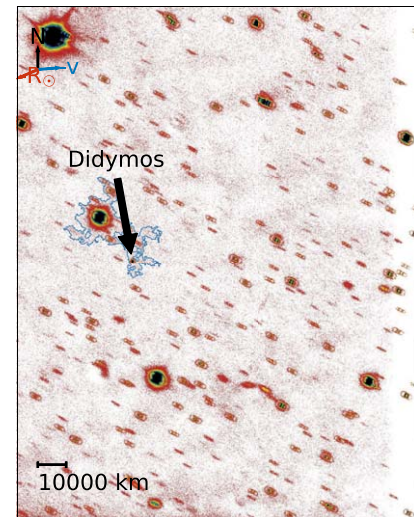
(a) 2023-01-25 20:00 – 22:11 (Midpoint: 2023-01-25 21:06)



(b) 2023-01-26 01:55 – 07:27 (Midpoint: 2023-01-26 04:41)



(c) 2023-01-26 21:17 – 01:13 (Midpoint: 2023-01-26 23:15)



(d) 2023-01-31 11:23 – 12:13 (Midpoint: 2023-01-31 11:48)

Figure 10. Median-combined stacked images of Didymos from 2023-01-24 to 2023-01-31 from the LCOGT network, along with annotated arrow pointing to Didymos. Note the larger scale bar of 10,000 km on these figures.

5.3. Light-curve Analysis

The combined ~ 150 days of LCOGT network data are shown on a linear scale in Figure 14 and on a logarithmic scale in Figure 17. For both of these plots we have also included the predicted magnitude from JPL Horizons. (The V magnitude has been computed for the geocenter, as the geocentric versus topocentric magnitudes for the many different telescopes in the network are negligible, and then converted to r' using the pre-impact $V - r$ color.)

Examination of the light curve in Figure 14 shows that the standard H, G model (Bowell et al. 1989) as calculated by Horizons (black curve) with $H_V = 18.11$, $G = 0.15$ overpredicts the magnitude in the range $T \sim 20\text{--}80$ days post-impact. Using an $H_V = 18.16$, $G = 0.2$ model (Pravec et al. 2012) produces a slightly worse result during the period from $T + 15\text{--}80$ days after impact, as shown in Figure 18.

As found by Moskovitz et al. (2024), we also find that an H, G_1, G_2 model (Muinonen et al. 2010; Penttilä et al. 2016)

produces a better match to the data in some areas but not all. To construct this model, we used the $G_1, G_2 = 0.84, 0.05$ as reported by Hasselmann et al. (2023), along with an $H_r = 17.94$ magnitude from JPL Horizons (and converted using the pre-impact $V - r$ color). We used *sppy* (Mommert et al. 2019) to evaluate the existing model parameters above, and the results are also shown in Figures 14 and 17 as the blue lines.

This better match to the data in some areas is seen in Figure 18, where we show the behavior of Didymos's magnitude and the behavior of the two H, G models, along with the H, G_1, G_2 model, over this time period of 15...130 days post impact, which covers the maxima ($\alpha \sim 76^\circ$) and minima ($\alpha \sim 6.5^\circ$) of the solar phase angle, α .

We also used *sppy* to perform an independent fit to all of our LCOGT data from 2022-07-05 to 2023-02-25 ($T - 83.9\text{...} + 151.3$ days before/after impact), excluding a time period from the time of impact to 30 days after the time of impact, to determine new values for H_r, G_1, G_2 . The results of this fit were $H_r = 18.05$, $G_1 = 0.98$, $G_2 = 0.02$, as shown in Figure 19, and show small

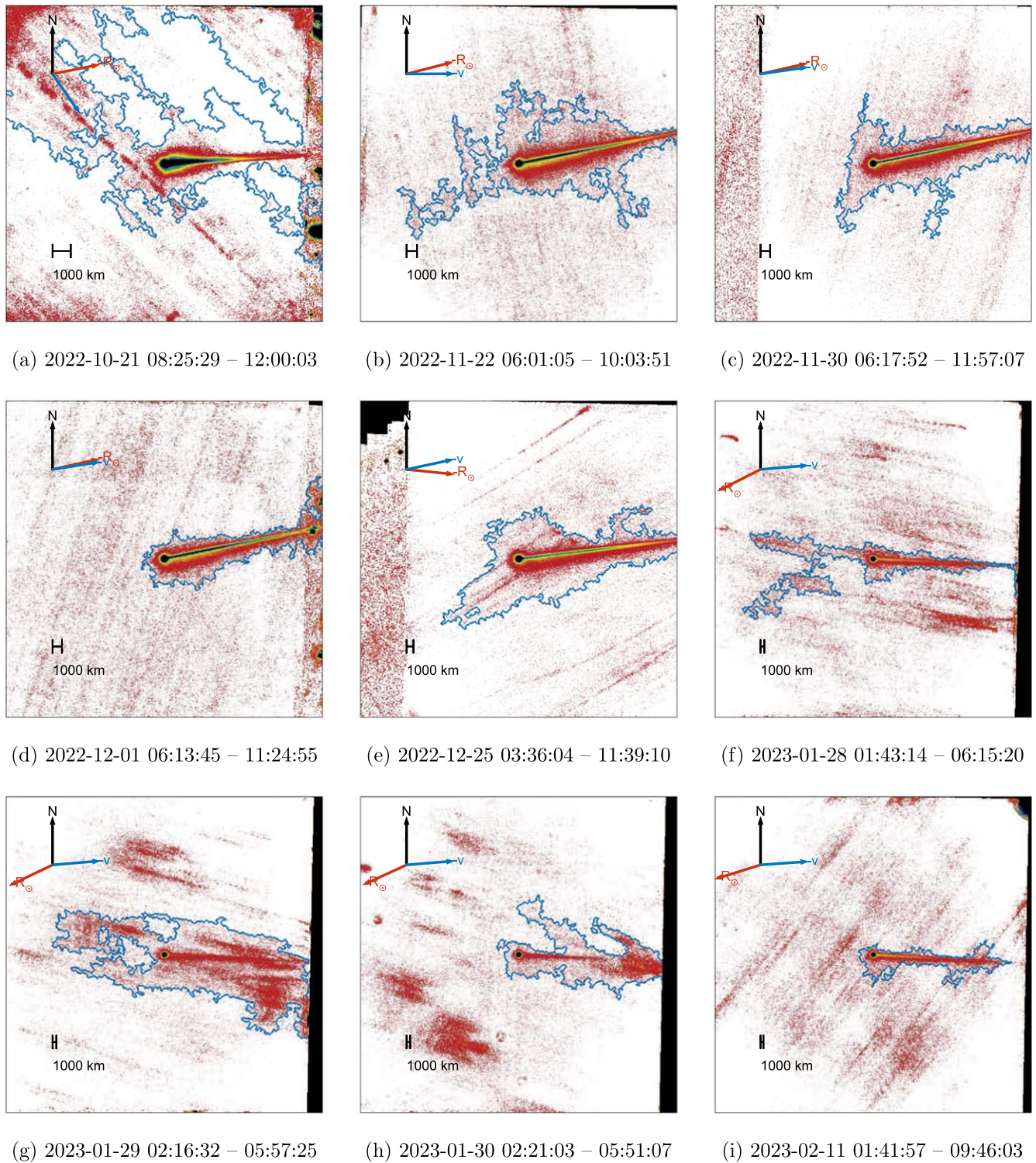
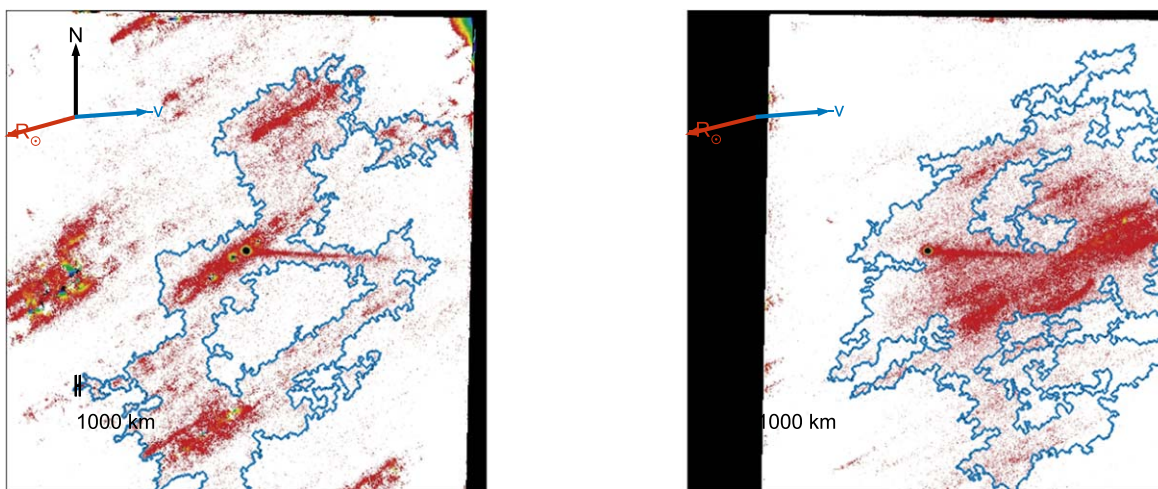


Figure 11. Median-combined stacked images of Didymos from 2022-10-21 to 2023-02-11 at MRO.

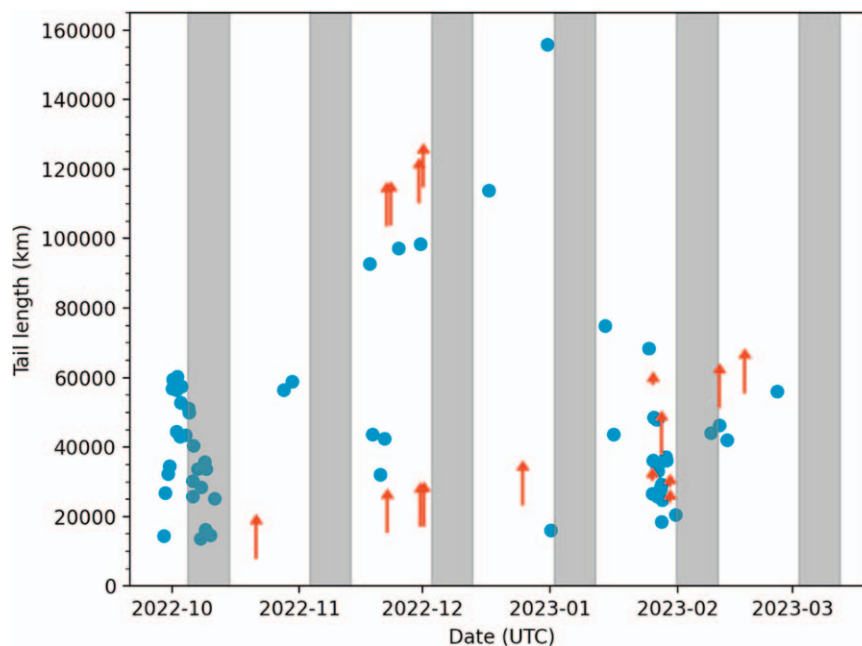
differences from the values listed above from Hasselmann et al. (2023), given the uncertainties of the fitting. In order to investigate the sensitivity and uncertainties of the fitted parameters, we used *emcee* (Foreman-Mackey et al. 2013) to perform a Markov Chain Monte Carlo (MCMC) analysis of the fitted model. We used loose priors of $17.5 \leq H \leq 20.5$ based on previous determinations for Didymos and the constraints $0.0 \leq G_1, G_2 \leq 1.0$, as well as an inequality constraint, $0 \leq 1 - G_1 - G_2 \leq 1$, required by the H, G_1, G_2 model. We used 100 walkers, each with 5000 iterations and 50

iterations of burn-in for the MCMC sampler run, to investigate the correlations between and determine the uncertainties on our parameter estimations. These are visualized as the 1D and 2D spreads between the parameters we are testing in Figure 20. Based on the 16th, 50th (median), and 84th percentiles of the samples in the marginalized distributions of the parameters, we find estimated 1σ uncertainties on each of the H, G_1, G_2 parameters of ± 0.002 . Both the original Hasselmann et al. (2023) model and our newly fit model show a poor fit at $\alpha < 20^\circ$ and are systematically



(a) 2023-02-17 07:05:14 – 10:28:01

(b) 2023-02-25 03:09:22 – 07:54:21

Figure 12. Median-combined stacked images of Didymos from 2023-02-17—2023-02-25 at MRO.**Figure 13.** Plot of the projected Didymos tail length (in km) from manual measurements (blue points) along with lower limits (red upward-pointing arrows) as a function of time. The time within ± 5 days of a full moon is shown by the gray vertical shaded area, as this will lead to brighter background and shorter measured tail lengths.

brighter than the data in this region, corresponding to the similar behavior seen during this period of smallest phase angles from $T \sim 90$ to 110 days post-impact in Figure 18.

In addition, we performed a separate fit using the same H_r , G_1 , G_2 model to the limited amount of our pre-impact data, but the limited phase coverage ($\alpha \sim 20^\circ \text{irc} \dots 50^\circ$) resulted in a poorly constrained and unphysical fit with $H_r \sim 17.1$, which would imply a diameter for Didymos of ~ 1.3 km, approximately double the well-determined diameter.

Also visible in Figure 19 for the data in the 30-day window following impact (orange circles) that were excluded from the phase-curve fit is the so-called “8-day bump” at $\alpha \sim 66$. This deviation from the smooth linear decrease in brightness was

also seen in data sets from other telescopes (Kareta et al. 2023; Lin et al. 2023; Rožek et al. 2023) and is thought to be due to large boulders recolliding within the system and producing an additional release of fine-grained material. This is also supported by analysis and modeling of the tail and extended ejecta cloud, which suggests a secondary impact that could have produced the second tail seen in some of the higher-resolution images (Lin et al. 2023; Moreno et al. 2023). Examining our combined stacks for the dates around this time does not provide any obvious evidence for a second tail structure. It is possible that further fine-tuning of the stacking parameters to produce cleaner images with less contamination from background field stars, combined with more sophisticated

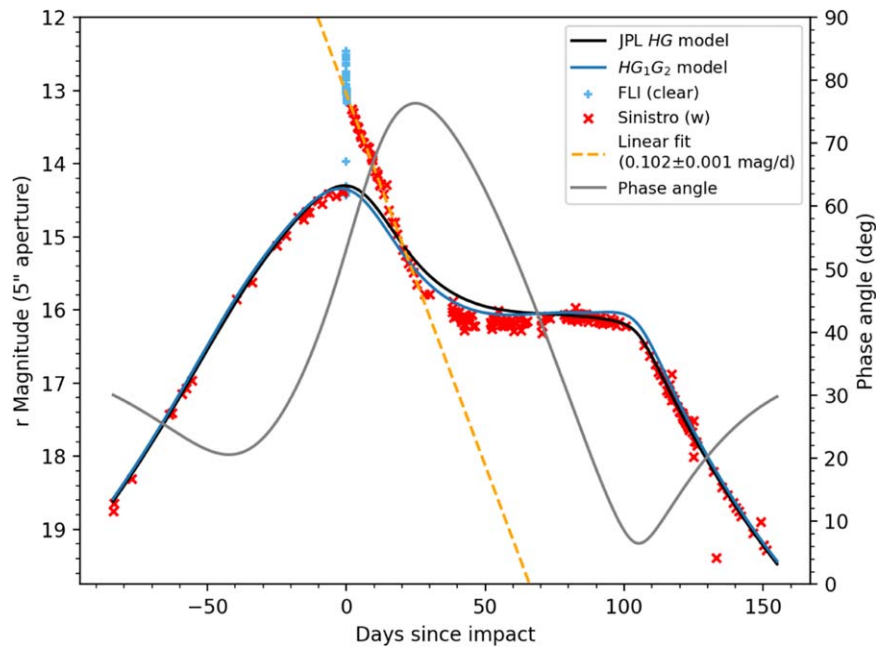


Figure 14. The magnitude of (65803) Didymos over the full time span of available data on a linear scale. The main Sinistro 1 m data from the light-curve and tail monitoring blocks, supplemented by the educational user data sets, are shown as the red crosses. The FLI clear filter data from the time of impact are shown as blue plus signs. A linear fit to the declining brightness of the Didymos system following impact is shown as the orange dashed line, along with a JPL Horizons $H(V)$, G model (black line) converted using the $V - r$ color and the H, G_1, G_2 model (blue line) with the parameters of Hasselmann et al. (2023).

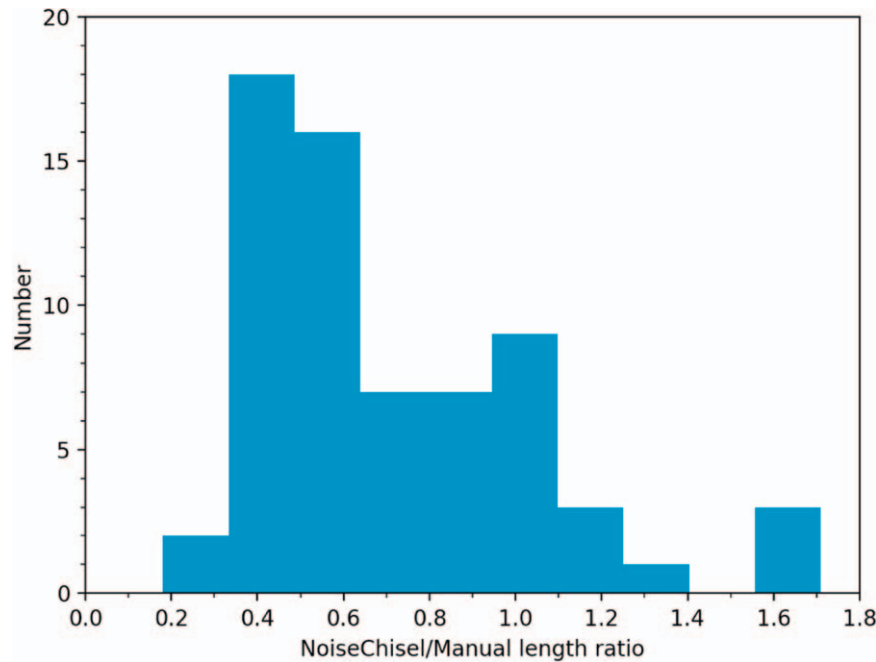


Figure 15. Ratio of the Didymos tail length measured with NoiseChisel to the manually measured length.

image-processing techniques than NoiseChisel provides, could potentially allow detection of the second tail in the LCOGT data.

Data over the first 30 days following impact presented by Kareta et al. (2023) showed a steady linear decline in brightness, with this reaching a turning point around 28 days after impact. It appears from our data analysis (see Figure 18) that the LCOGT data also show this turning point at $T \sim 28$ days, but the measured brightness of Didymos fell

below the model predictions for the next ~ 60 days before returning to the predicted baseline magnitude from JPL Horizons (and converted using the pre-impact $V - r$ color) around 80 days following the impact. The JPL Horizons H, G model provides the better fit to the late-time light curve, particularly during the period of lowest phase angle at $T 115$ days post-impact, but overpredicts the magnitude compared to the H, G_1, G_2 model in the region of $T \sim 25...65$ days.

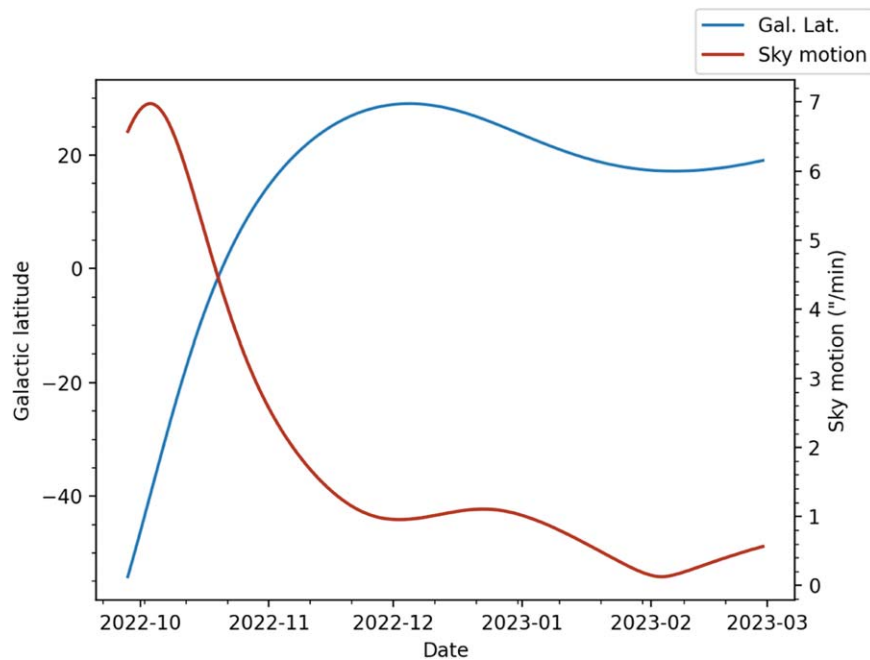


Figure 16. The galactic latitude (blue line, left-hand scale; used as a proxy for the stellar density within the observing fields) and the rate of on-sky motion of Didymos (red line, right-hand scale) over the course of the observing campaign.

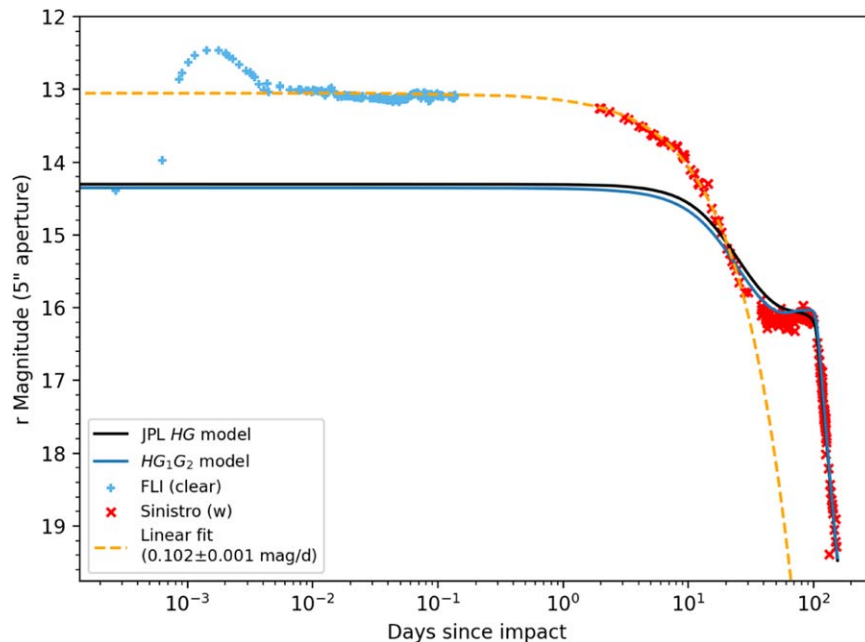


Figure 17. The magnitude of (65803) Didymos as a function of time after the DART impact but on a logarithmic timescale. The same fit to the declining brightness (orange line) and the theoretical H, G and H, G_1, G_2 models (black and blue lines, respectively, as in Figure 14) are also shown.

6. Conclusions

We have described and analyzed the ~ 8 months of data that were collected with the LCOGT network across the globe as Didymos moved from the Southern to Northern Hemisphere before fading from the view of these telescopes at the end of 2023 February. The light-curve data show the large initial rise in brightness in the minutes after impact and a linear decline of $\sim 0.102 \text{ mag day}^{-1}$ interrupted by a brief brightening for the “8-day bump,” before resuming the decline lasting for a total of ~ 28 days before returning to baseline magnitude (as predicted by JPL Horizons) around $\sim 2022-12-15$ after 80 days. The light

curve was not well modeled with the H, G model in all areas, and we find that an H, G_1, G_2 model overall produced a better fit to more of the light curve but overpredicted the system magnitude during the period of smallest phase angles from $T \sim 90$ to 110 days following impact. In this region, the standard $H, G = 0.15$ model was found to fit the light curve better than the original or refitted H, G_1, G_2 models.

In addition to analyzing the LCOGT data for long-term photometric analysis, we also performed an analysis of the impact-induced ejecta and tail and supplemented the LCOGT network data with additional data sets obtained with the larger

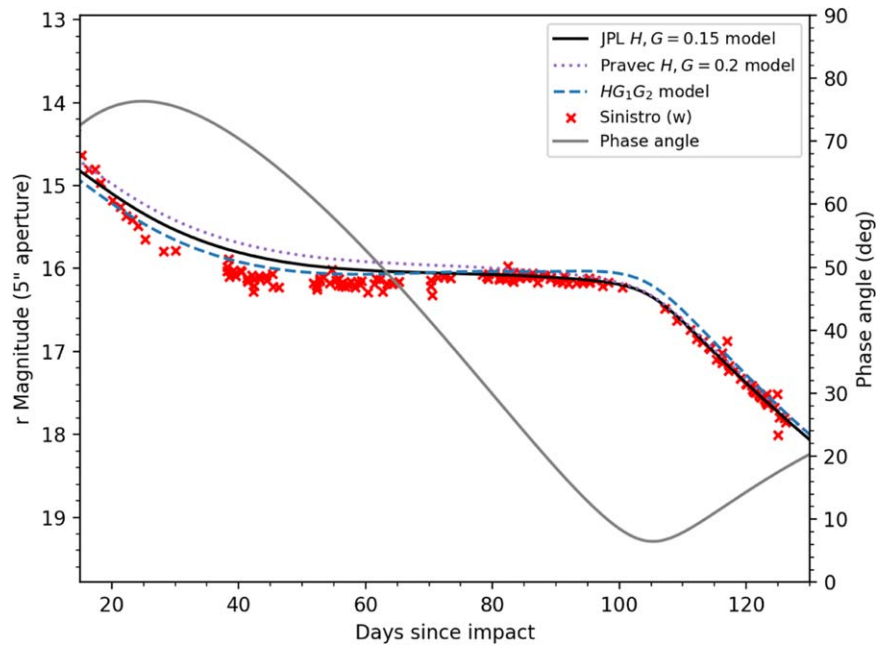


Figure 18. The comparison between the magnitude of (65803) Didymos and the $H, G = 0.15$ (black line), the Pravec et al. $H, G = 0.2$ (purple dotted line), and the H, G_1, G_2 model (blue dashed line) over the time span from $T + 15$...130 days after impact. Also plotted (right-hand scale) is the solar phase angle over the time period.

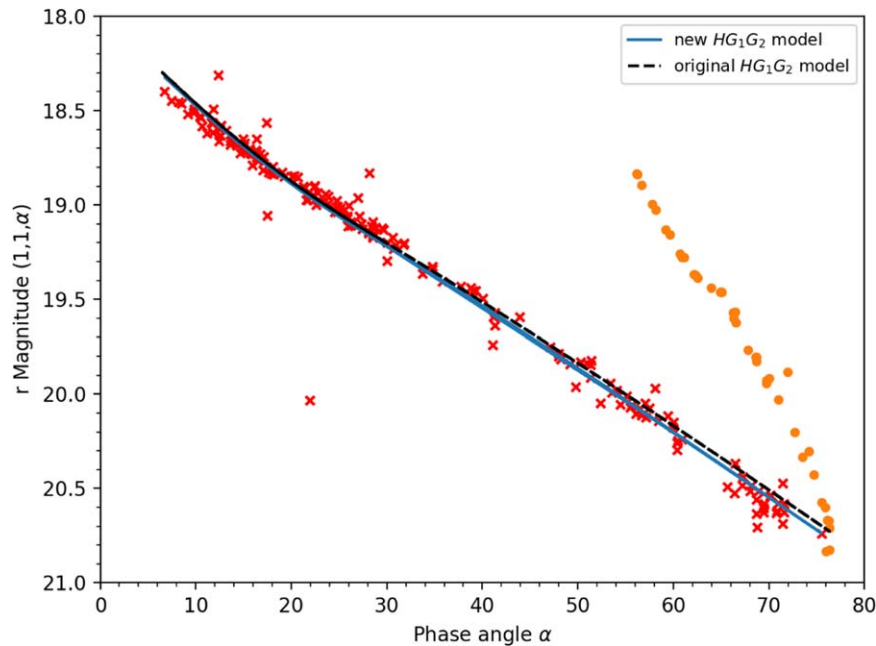


Figure 19. The reduced magnitude $H(1, 1, \alpha)$ of (65803) Didymos as a function of phase angle α . The model was fit to the data set (red crosses), which excluded the 30-day period following the time of impact; data from this period after impact are shown as the orange circles and clearly show a different behavior with time/phase than expected from the original (black dashed line) or newly fit H, G_1, G_2 model (blue line).

2.4 m MRO telescope. These MRO data sets were useful at the end of the Didymos observing campaign in 2023 February, as they went substantially deeper than the much shorter tail monitoring blocks that were being carried on the smaller LCOGT network 1 m telescopes at the time. We used Gnuastro and NoiseChisel to perform stacking of images and detection and measurement of extended morphological features produced by the DART impact. Combined with manual measurements of the tail extent, this enabled

measurement of the growing tail over the first few days following the DART impact, as well as longer-term monitoring of the growth and evolution of the tail over the months following impact. This showed that the tail initially grew rapidly over the first ~ 10 days before then continuing to evolve and grow in length over the 3 months following impact. This was followed by an apparent decrease in length due to the changing geometry as the phase angle underwent rapid evolution in early 2023.

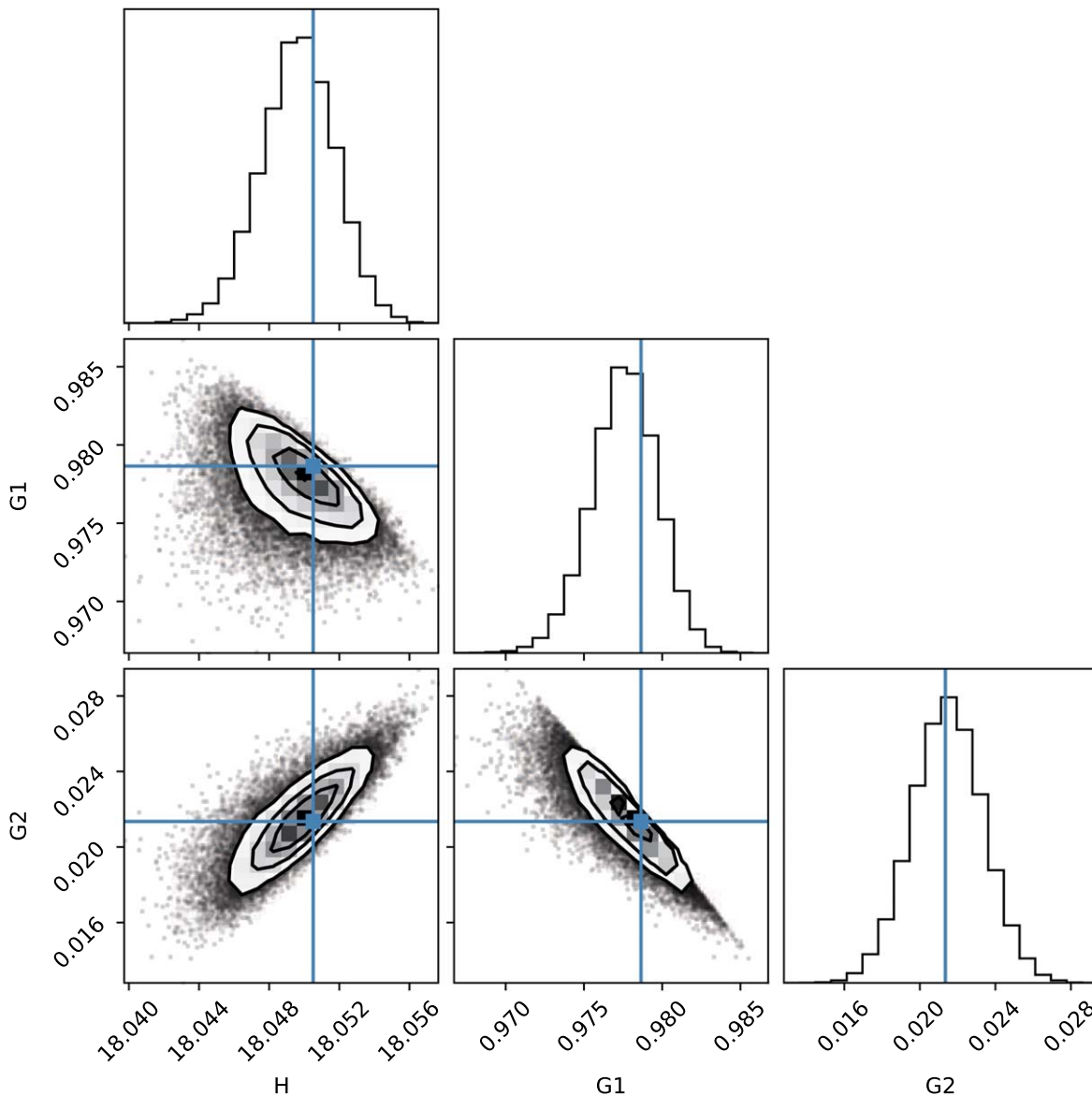


Figure 20. The MCMC corner plot showing the 1D and 2D projections of the posterior probability distributions of the parameters from the fit to the H , G_1 , G_2 model, along with the best-fit parameters (blue lines and points).

Comparing the tail lengths found by *NoiseChisel* and the manual measurement technique showed a general trend for the *NoiseChisel* to underpredict the manually measured tail length, but the value of this ratio showed considerable variation with time and observing conditions. In addition, there were a considerable number of cases where the *NoiseChisel* detection contour around Didymos suffered from contamination from background star trails, limiting the application of this tool in “hands-off” automated application without considerable application of additional optimization of the stacking strategy and tuning of the *NoiseChisel* parameters for particular subsets of the data. The application of this technique to large, moderately homogeneous data sets spanning a wide variety of observing conditions will need to be the subject of extra work in order for it to be applied automatically to reliably detect and measure ejecta cloud and tail-like features from outbursts as part of an automated system for future sky surveys such as Rubin Observatory’s Legacy Survey of Space and Time (LSST).

Acknowledgments

This work was supported by the DART mission, NASA contract No. 80MSFC20D0004. Parts of this work (the development of NEOexchange) were funded by NASA NEOO grants NNX14AM98G and 80NSSC18K0848 to LCO. This work makes use of observations from the Las Cumbres Observatory Global Telescope network. We thank all of the staff at the observatory and the remote telescope sites for their assistance in making these observations possible. In addition, we thank Rachel Street for the assistance with carrying out the MCMC analysis of phase-curve data. This paper is based on observations made with the MuSCAT3 instrument, developed by the Astrobiology Center and under financial supports by JSPS KAKENHI (JP18H05439) and JST PRESTO (JPMJPR1775), at Faulkes Telescope North on Maui, HI, operated by the Las Cumbres Observatory. The Comet Chasers school outreach project is funded by the UK Science and Technology Facilities Council through the DeepSpace2DeepImpact Project, the Royal Astronomical Society, the Open

University, and Cardiff University. It accesses the LCOGT telescopes through the Faulkes Telescope Project (FTPE-PO2014A-004), which is partly funded by the Dill Faulkes Educational Trust. Observations include those made by students from St Marys Catholic Primary School (Bridgend), White Rose Primary School (New Tredegar), Radnor Primary School (Cardiff), Montgomery Church in Wales Primary School (Montgomery), Ysgol Gyfun Gymraeg Bro Edern (Caerdydd), Rhiwbina Primary School (Cardiff), Poole Grammar School (Poole), Abbey Grange Academy (Leeds), and Juozas Urbys School (Kaunas, Lithuania), and at the National Eisteddfod of Wales.

The data sets are available at the Planetary Data System (PDS) Small Bodies Node (SBN) in the DART Telescopic Observation Archive v2.0 data bundle doi:10.26007/p055-ce48. The data analyzed in this paper came from six data products from this bundle:

1. [urn:nasa:pds:dart_teleobs:data_lcoctrav::1.0](https://pds.nasa.gov/data/atlas/lco/urn:nasa:pds:dart_teleobs:data_lcoctrav::1.0)
doi:10.26007/atbp-8p57
2. [urn:nasa:pds:dart_teleobs:data_lcoctcal::1.0](https://pds.nasa.gov/data/atlas/lco/urn:nasa:pds:dart_teleobs:data_lcoctcal::1.0)
doi:10.26007/cned-dh53
3. [urn:nasa:pds:dart_teleobs:data_lcoctddp::1.0](https://pds.nasa.gov/data/atlas/lco/urn:nasa:pds:dart_teleobs:data_lcoctddp::1.0)
doi:10.26007/gnwj-cz77

4. [urn:nasa:pds:dart_teleobs:data_mroraw::1.0](https://pds.nasa.gov/data/atlas/lco/urn:nasa:pds:dart_teleobs:data_mroraw::1.0)
doi:10.26007/k2aj-1g81
5. [urn:nasa:pds:dart_teleobs:data_mrocal::1.0](https://pds.nasa.gov/data/atlas/lco/urn:nasa:pds:dart_teleobs:data_mrocal::1.0)
doi:10.26007/s0bn-9941
6. [urn:nasa:pds:dart_teleobs:data_mroddp::1.0](https://pds.nasa.gov/data/atlas/lco/urn:nasa:pds:dart_teleobs:data_mroddp::1.0)
doi:10.26007/eety-xf47

and the raw frames and BCD (BANZAI-processed) products are available at the LCOGT Science Archive at <https://archive.lco.global> using proposal codes KEY2020B-009, LCO2022A-003, LCO2022B-006, and LCO2023A-005 and educational user proposal codes FTPEPO2014A-004 and HAW2022B-001.

Facility: LCOGT (1 m Sinistro, 1 m FLI), FTN, FTS, MRO.

Software: astropy (Astropy Collaboration et al. 2013, 2018, 2022), calviacat (Kelley & Lister 2022) emcee (Foreman-Mackey et al. 2013) Gnuastro (Akhlaghi & Ichikawa 2015; Akhlaghi 2018, 2019) IRAF (Tody 1986) SCAMP (Bertin 2006), Source Extractor (Bertin & Arnouts 1996).

Appendix Observation Tables

This appendix provides details of the individual observation blocks and nights of observation for the LCOGT Network (Table 2) and MRO (Table 3), respectively.

Table 2
Table of Observations for (65803) Didymos with LCOGT

Block Start	Block End	Site	Telclass	MPC Site Code	Filters	Num Exposures
2022-07-05 01:46	2022-07-05 01:55	cpt	1m0	K93	<i>r'</i>	6/6
2022-07-05 05:53	2022-07-05 06:02	lsc	1m0	W87	<i>w</i>	4/4
2022-07-11 13:35	2022-07-11 13:47	coj	1m0	Q64	<i>w</i>	5/5
2022-07-12 05:09	2022-07-12 05:51	lsc	1m0	W85	<i>i'</i>	10/10
2022-07-22 00:10 ^a	2022-07-22 16:31	cpt	1m0	Q64	<i>i'</i>	46/46
			⋮			
2023-02-22 07:50	2023-02-22 08:07	elp	1m0	V39	<i>w</i>	4/4
2023-02-23 02:15	2023-02-23 02:33	elp	1m0	V39	<i>w</i>	4/4
2023-02-24 04:45	2023-02-24 05:03	elp	1m0	V39	<i>w</i>	4/4
2023-02-25 06:13	2023-02-25 06:26	elp	1m0	V39	<i>w</i>	3/4

Note. Each row represents a single-night, single-site, single-telescope light curve or tail monitoring block. The columns list the observing circumstances for each block: the UTC start and end of each exposure block, the LCOGT site code and telescope class, the MPC site code, the filters used, and the number of exposures taken/scheduled. The horizontal line splits pre-impact and post-impact data sets.


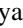
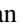





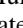
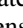
^a Observations that were collected on the LCOGT network but not analyzed in this paper.

(This table is available in its entirety in machine-readable form.)

Table 3
Table of Observations for (65803) Didymos with MRO

Block Start	Block End	Site	Telclass	MPC Site Code	Filters	Num Exposures
2022-10-11 08:49	2022-10-11 12:03	MRO	2m4	H01	<i>R,V</i>	371/371
2022-10-21 08:25	2022-10-21 12:00	MRO	2m4	H01	<i>R</i>	257/257
2022-11-22 06:01	2022-11-22 10:03	MRO	2m4	H01	<i>R</i>	289/289
2022-11-30 06:17	2022-11-30 11:57	MRO	2m4	H01	<i>R</i>	412/412
2022-12-01 06:13	2022-12-01 11:24	MRO	2m4	H01	<i>R</i>	290/290
2022-12-25 03:36	2022-12-25 11:39	MRO	2m4	H01	<i>R</i>	567/567
2023-01-28 01:43	2023-01-28 06:15	MRO	2m4	H01	<i>R</i>	205/205
2023-01-29 02:16	2023-01-29 05:57	MRO	2m4	H01	<i>R</i>	152/152
2023-01-30 02:21	2023-01-30 05:51	MRO	2m4	H01	<i>R</i>	104/104
2023-02-11 01:41	2023-02-11 09:46	MRO	2m4	H01	<i>VR</i>	276/276
2023-02-17 07:05	2023-02-17 10:28	MRO	2m4	H01	<i>VR</i>	43/43
2023-02-25 03:09	2023-02-25 07:54	MRO	2m4	H01	<i>VR</i>	57/57

ORCID iDs

Tim Lister  <https://orcid.org/0000-0002-3818-7769>
 William Ryan  <https://orcid.org/0000-0002-9226-4956>
 Eileen Ryan  <https://orcid.org/0000-0001-6921-9877>
 Edward Gomez  <https://orcid.org/0000-0001-5749-1507>
 Liz Phillips  <https://orcid.org/0000-0003-0171-1878>
 Agata Rożek  <https://orcid.org/0000-0003-2341-2238>
 Helen Usher  <https://orcid.org/0000-0002-8658-5534>
 Brian P. Murphy  <https://orcid.org/0000-0002-8137-5132>
 Joseph Chatelain  <https://orcid.org/0000-0002-1278-5998>
 Sarah Greenstreet  <https://orcid.org/0000-0002-4439-1539>

References

- Akhlaghi, M. 2018, Gnuastro: GNU Astronomy Utilities, Astrophysics Source Code Library, ascl:1801.009
- Akhlaghi, M. 2019, arXiv:1909.11230
- Akhlaghi, M., & Ichikawa, T. 2015, *ApJS*, **220**, 1
- Astropy Collaboration, Price-Whelan, A. M., Lim, P., et al. 2022, *ApJ*, **935**, 167
- Astropy Collaboration, Price-Whelan, A. M., Sipőcz, B., et al. 2018, *AJ*, **156**, 123
- Astropy Collaboration, Robitaille, T. P., Tollerud, E., et al. 2013, *A&A*, **558**, A33
- Bertin, E. 2006, in ASP Conf. Ser. 351, *Astronomical Data Analysis Software and Systems XV*, ed. C. Gabriel et al. (San Francisco, CA: ASP), 112
- Bertin, E., & Arnouts, S. 1996, *A&AS*, **117**, 393
- Bowell, E., Hapke, B., Domingue, D., et al. 1989, in *Asteroids II*, ed. R. P. Binzel, T. Gehrels, & M. S. Matthews (Tucson, AZ: Univ. Arizona Press), 524
- Brown, T. M., Baliber, N., Bianco, F. B., et al. 2013, *PASP*, **125**, 1031
- Chabot, N., Rivkin, A. S., Cheng, A. F., et al. 2024, *PSJ*, **5**, 49
- Cheng, A. F., Agrusa, H. F., Barbee, B. W., et al. 2023, *Natur*, **616**, 457
- Daly, R. T., Ernst, C. M., Barnouin, O. S., et al. 2023, *Natur*, **616**, 443
- Fahnestock, E. G., Cheng, A. F., Ivanovski, S., et al. 2022, *PSJ*, **3**, 206
- Fitzsimmons, A., Berthier, J., Denneau, L., et al. 2023, *Asteroids, Comets, Meteors Conf.*, **2851**, 2452
- Flewellling, H. A., Magnier, E. A., Chambers, K. C., et al. 2020, *ApJS*, **251**, 7
- Foremán-Mackey, D., Hogg, D. W., Lang, D., & Goodman, J. 2013, *PASP*, **125**, 306
- Gaia Collaboration, Brown, A. G. A., Vallenari, A., et al. 2018, *A&A*, **616**, A1
- Hainaut, O. R., Kleyna, J., Sarid, G., et al. 2012, *A&A*, **537**, A69
- Hasselmann, P. H., Dotto, E., Deshapriya, J. D. P., et al. 2023, *Asteroids, Comets, Meteors Conf.*, **2851**, 2172
- Kareta, T., Thomas, C. A., Li, J.-Y., et al. 2023, *ApJL*, **959**, L12
- Kelley, M., & Lister, T. 2022, mkelley/calviacat: v1.3.0 Zenodo, doi:10.5281/zenodo.7019180
- Li, J.-Y., Hirabayashi, M., Farnham, T. L., et al. 2023, *Natur*, **616**, 452
- Lin, Z.-Y., Vincent, J.-B., & Ip, W.-H. 2023, *A&A*, **676**, A116
- Lister, T. A., Gomez, E., Chatelain, J., et al. 2021, *Icar*, **364**, 114387
- McCully, C., Volgenau, N. H., Harbeck, D. R., et al. 2018, *Proc. SPIE*, **10707**, 107070K
- Michel, P., Küppers, M., Bagatin, A. C., et al. 2022, *PSJ*, **3**, 160
- Mommert, M. 2017, PHOTOMETRYPIPELINE: Automated photometry pipeline, Astrophysics Source Code Library, ascl:1703.004
- Mommert, M., Kelley, M. P., de Val-Borro, M., et al. 2019, *JOSS*, **4**, 1426
- Moreno, F., Bagatin, A. C., Tancredi, G., et al. 2023, *PSJ*, **4**, 138
- Moreno, F., Campo Bagatín, A., Tancredi, G., Liu, P.-Y., & Domínguez, B. 2022, *MNRAS*, **515**, 2178
- Moskovitz, N., Thomas, C., Pravec, P., et al. 2024, *PSJ*, **5**, 35
- Muinenen, K., Belskaya, I. N., Cellino, A., et al. 2010, *Icar*, **209**, 542
- Narita, N., Fukui, A., Yamamuro, T., et al. 2020, *Proc. SPIE*, **11447**, 114475K
- Opitom, C., Murphy, B., Snodgrass, C., et al. 2023, *A&A*, **671**, L11
- Penttilä, A., Shevchenko, V. G., Wilkman, O., & Muinenen, K. 2016, *P&SS*, **123**, 117
- Pravec, P., Harris, A. W., Kušnirák, P., Galád, A., & Hornoch, K. 2012, *Icar*, **221**, 365
- Rivkin, A. S., Chabot, N. L., Stickle, A. M., et al. 2021, *PSJ*, **2**, 173
- Rożek, A., Snodgrass, C., Jørgensen, U. G., et al. 2023, *PSJ*, **4**, 236
- Snodgrass, C., Tubiana, C., Vincent, J.-B., et al. 2010, *Natur*, **467**, 814
- Thomas, C. A., Naidu, S. P., Scheirich, P., et al. 2023, *Natur*, **616**, 448
- Tody, D. 1986, *Proc. SPIE*, **627**, 733